Journal of Energy Storage 95 (2024) 112449

Contents lists available at ScienceDirect

Journal of Energy Storage

journal homepage: www.elsevier.com/locate/est

Review Article

MXene-polymer hybrid composites for advanced energy storage: Insights into supercapacitors and batteries

Hafiz Taimoor Ahmed Awan [a,1], Muhammad Amirul Aizat Mohd Abdah [a,b,1], Maida Mehar [c], Rashmi Walvekar [d,e], Vishal Chaudhary [f], Mohammad Khalid [a,g,h,*], Ajit Khosla [i,**]

[a] Sunway Centre for Electrochemical Energy and Sustainable Technology (SCEEST), School of Engineering and Technology, Sunway University, No. 5, Jalan Universiti, Bandar Sunway, 47500 Selangor Darul Ehsan, Malaysia
[b] Department of Chemistry, Faculty of Science, Universiti Teknologi Malaysia, 81310 Johor Bahru, Johor, Malaysia
[c] Department of Physics, University of Agriculture, Faisalabad, Punjab 38000, Pakistan
[d] Faculty of Innovation and Technology, School of Engineering, Chemical Engineering Programme, No.1 Jalan Taylor's, Taylor's University Malaysia, 47500 Subang Jaya, Selangor, Malaysia
[e] Chitkara Centre for Research and Development, Chitkara University, Himachal Pradesh 174103, India
[f] Physics Department & Research Cell, Bhagini Nivedita College, University of Delhi, Delhi 110043, India
[g] James Watt School of Engineering, University of Glasgow, Glasgow, G12 8QQ UK
[h] University Centre for Research and Development, Chandigarh University, Mohali, Punjab, 140413, India
[i] School of Advanced Materials and Nanotechnology, Xidian University, Xi'an, Shaanxi Province 710126, China

ARTICLE INFO

Keywords:
MXene
Energy storage technology
Supercapacitor
Battery
Polymer composite
2D material

ABSTRACT

Modern energy storage technologies are an active area of research because of their increasing demand in electronic gadgets, automotive, and electric vehicle applications. Supercapacitors and batteries substantially meet such needs due to their internal surface area, high surface-to-volume ratio, as well as high energy density and mobility of the two-dimensional (2D) materials. As a result, 2D materials—particularly MXene, comprised of carbide nitride and corresponding combinations—are ideal options for energy storage devices and applications. The present review focuses on MXene and corresponding composites—especially polymer-based. We also provide an overview of MXene and polymer harnessing methods, as well as corresponding, e.g., electrical and mechanical features. The use of MXene and polymeric materials in batteries and supercapacitors—as well as upcoming difficulties and results—are all covered in the context of energy storage applications.

1. Introduction

Global energy needs have exponentially increased because of rapid industrialization in the decades after World War II. Accordingly, industrialization demand has rapidly increased, which has resulted in the expansion of power consumption, along with rising living conditions, which has further increased energy demand for personal use. Until the start of the 20th century, most fossil fuel resources were used to supply power. The depletion of fossil fuel reserves, coupled with the growth of the global population and the environmental pollution resulting from mining and hydrocarbon consumption, have collectively intensified the need for energy storage solutions that are renewable and sustainable [1]. These global problems indicate the challenges of ongoing dependence on fossil fuels as a source of energy. Therefore, to meet global energy needs, the scientific community is developing modern technology to allow renewable energy sources to be maximally utilized. In addition to energy conversion technologies, energy storage devices are also required because solar, wind and tidal energy are weather-dependent. To address climate change, research is underway on inexpensive, ecologically friendly energy storage technologies, including batteries and supercapacitors. Alternatively, energy storage devices are frequently applied in the medical industry, defence, transportation (such as electric cars), and portable electronic appliances (such as watches, cameras, smartphones, and laptops) [2,3]. Numerous energy storage devices have been developed since the discovery of electricity, each with unique benefits and drawbacks. Renewable energy

* Correspondence to: M. Khalid, James Watt School of Engineering, University of Glasgow, Glasgow, G12 8QQ UK.
** Corresponding author.
E-mail addresses: mohammad.khalid@glasgow.ac.uk (M. Khalid), ajitkhosla@xidian.edu.cn (A. Khosla).
[1] Equal contributing authors.

https://doi.org/10.1016/j.est.2024.112449
Received 10 March 2024; Received in revised form 2 May 2024; Accepted 2 June 2024
Available online 20 June 2024

sources can be readily integrated with energy storage technologies (EST), which quickly store or release energy in response to system demands. Moreover, large-scale ESTs can serve as reserve capacity for conventional generators, thus reducing carbon emissions.

There are multiple EST variations for different uses (Fig. 1); ESTs are generally distinguished from one another based on their storage mechanism (energy density, power density, discharge time, or reaction time; depending on their function) or the services they can provide. ESTs can be categorized into five groups: mechanical energy storage, electrochemical energy storage (EcES), electrical energy storage (EES), chemical energy storage (CES), and thermal energy storage. The following subsections mostly concentrate on CES (solar fuels), EcES (battery energy storage), EES (electrostatic/redox energy storage), and applications. A brief history of EST development is required to provide a historical perspective on these designs (Fig. 2). EST development started in 1745 when Pieter van Musschenbroek invented the Leyden Jar, the precursor of the current battery. The jar was used in several early electrical experiments and, in principle, stored electrical energy similar to a capacitor. Its development was essential for understanding electricity [4].

The history of battery development spans centuries, with numerous substantial advancements contributing to the field of electronics and energy storage. Alessandro Volta is credited with developing the first electrical battery in 1800, which consisted of two metal plates submerged in a chemical solution. [5] In 1839, Sir William Robert Grove introduced fuel cells and noted that the first voltaic battery consisted of four pairs of zinc and platinum foil plates [6]. In 1859, Gaston Planté developed a lead-acid battery, which could be recharged by sending a reverse current through it. Thomas Edison's nickel-iron battery was utilized in electric vehicles until the 1920s and subsequently served as a backup power source for mines and railroads until the mid-1900s [7]. In 1896, William W. Jacques reported on his efforts to generate "electricity direct from coal." Waldemar Jungner created the nickel-cadmium secondary battery in 1899, which was sufficiently durable to withstand harsh operating conditions such as overcharging, over-discharging, and prolonged cycling [8]. William Dubilier's invention of the "condenser" (later termed the capacitor) using mica, a glassy crystal, led to numerous pioneering advances in electronics and radio. Thomas Edison developed the first alkaline battery in 1914 for use in electric vehicles but was unable to release it due to technical difficulties.

In 1939, Francis Thomas Bacon created the first alkali electrolyte fuel cell, utilizing potassium hydroxide as the electrolyte and porous "gas-diffusion" electrodes. In 1960, the film and foil capacitor was introduced, consisting of two metal foil electrodes separated by a plastic film typically composed of polypropylene. The electrolytic capacitor and pseudo-capacitance in ruthenium oxide were developed in subsequent years. Stanford Ovshinsky obtained a nickel metal hydride battery patent while researching hydrogen storage materials in 1976 [8].

Finally, in 1991, the first commercial lithium-ion battery (LIB) was produced by Asahi Kasei in collaboration with Sony Corporation [9]. This marked a substantial milestone in battery technology and facilitated the development of high-performance rechargeable batteries that are widely used today.

After the development of the first SC—also known as an ultracapacitor—in 1992, the majority of SC research has focused on increasing the energy density of these devices by creating hybrid and asymmetric SCs [10,11]. In 2001, the Goodenough group made additional strides in developing lithium iron phosphate ($LiFePO_4$). Additionally, due to innovations in experimental methodologies and mathematical modelling, great progress has been made toward a better understanding of the electrochemical performance of LIBs as well as their deterioration, safety, production, and recyclability. With the development of smart battery technology, the need to monitor batteries and give customers a better and safer experience became apparent. By incorporating sensing, communication, and controller hardware into the battery, smart battery technology aims to transform the LIB into a mechatronic device rather than merely a passive component. With improved safety, fault-tolerant operation, a longer lifespan, and software reconfiguration for secondary use, an integrated battery solution can be produced. Even though LIBs have been commercialized for use in portable electronics, intensive research on high-energy-density anode materials continues to meet the constantly increasing high energy demand for future advanced self-powering smart portable electronics and large-scale applications, such as electric vehicles and power grids. Fig. 3a shows the performance trend for SCs and rechargeable batteries in terms of energy density (Li-ion). Batteries and SCs have been greatly

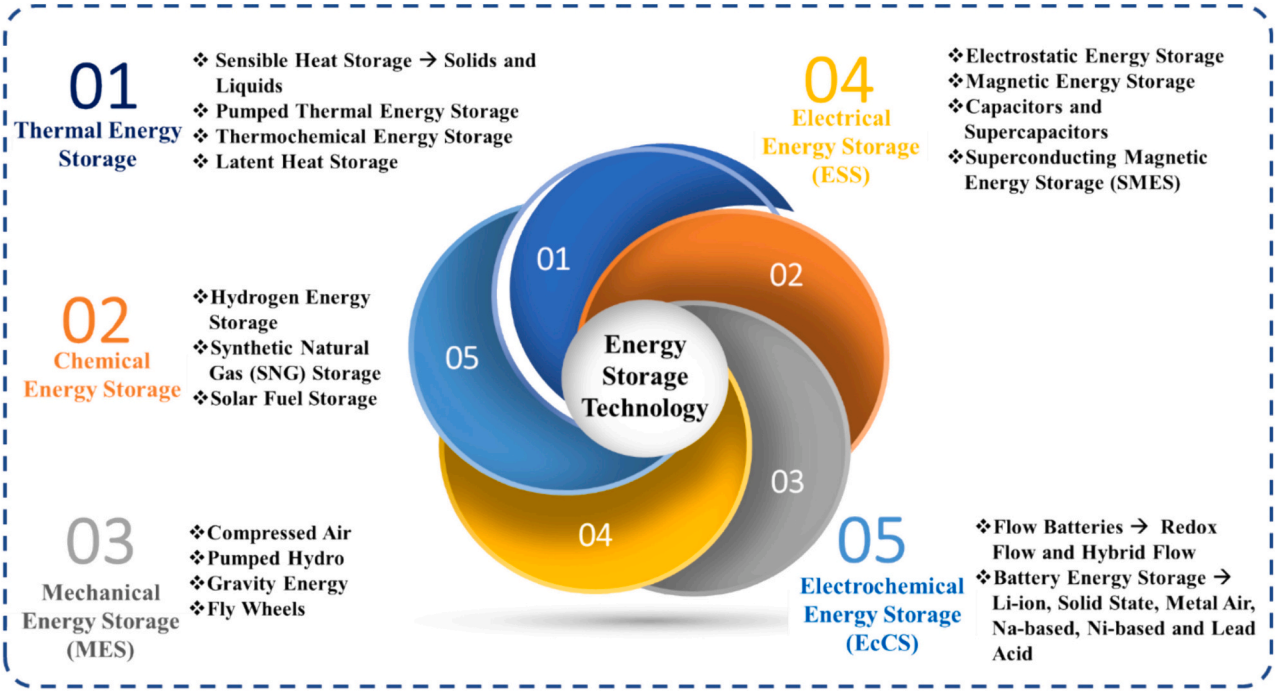

Fig. 1. Organogram of various energy storage systems.

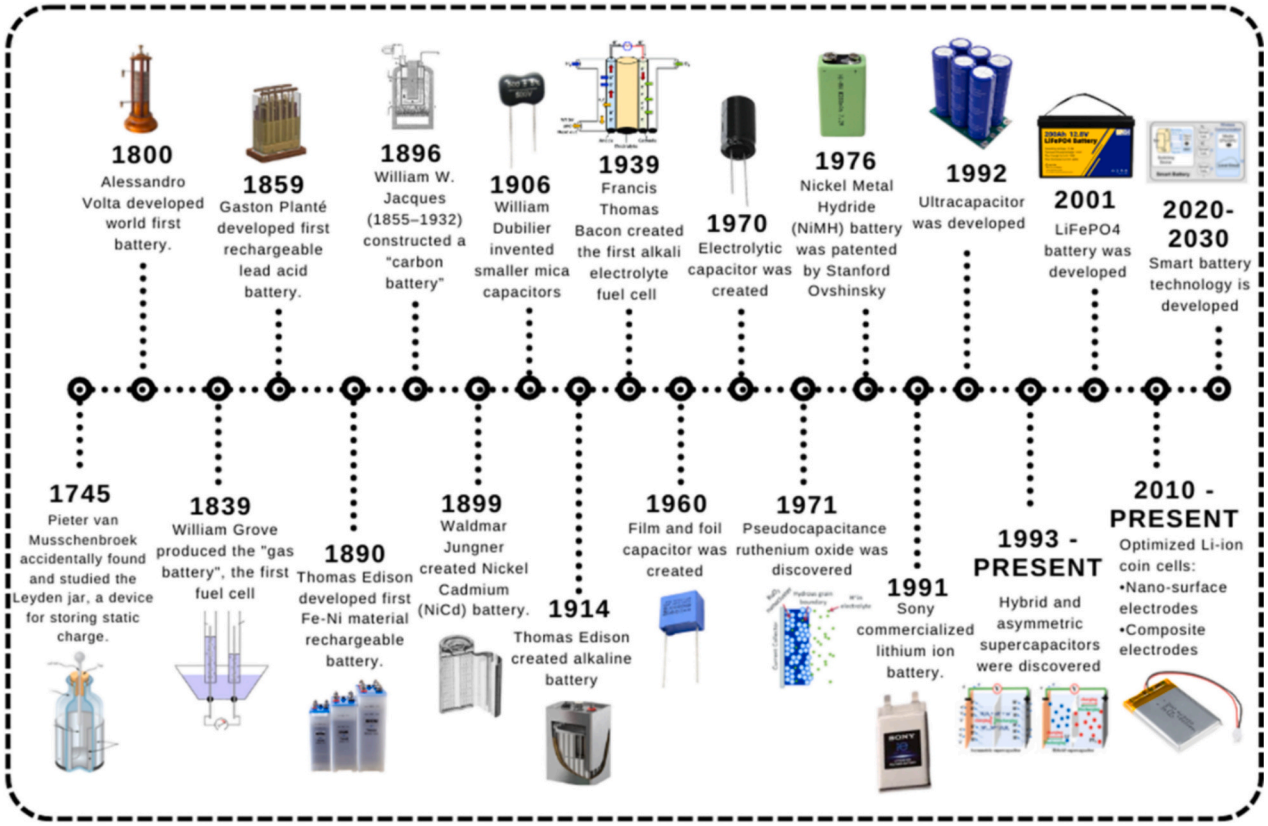

Fig. 2. Brief timeline of the production of energy storage technology.

enhanced in terms of energy production since the beginning of 1990. The quality of the electrode materials, a substantial EST component, is essential for determining the total electrochemical performance [12]. This renders creating novel, high-performance electrode materials with high conductivity and charge storage capacity crucial. Since their discovery in 2011, MXenes—a class of two-dimensional (2D) layered transition metal carbides, nitrides, or carbonitrides—has been recognized as a viable electrode material for EST [13,14]. MXene has several intriguing properties, including a strong electric conductivity that enhances rate performance and a large surface area that facilitates ion diffusion for redox reactions. In addition, hybridizing MXene with nanomaterial spacers (such as carbon materials [15], metal oxides [16,17], conducting polymers [18], black phosphorus [19,20], metal sulfides [21,22], and Si [23,24]) not only avoids restacking of MXene sheets but also introduces functionalization, which synergistically enhances its electrochemical performance. Because of these elements, MXenes are currently the subject of intense research among scientists working on energy storage applications. Fig. 3b shows a schematic of the annual growth in the number of publications devoted to MXene materials for energy storage applications. Over the past 10 years, MXene development for energy storage applications has advanced quickly. The most current advancements in MXene-based polymer composites for energy storage applications are thoroughly reviewed in this article. The principles of EST are first highlighted, including the many types of ESTs, the development of SCs and LIBs, as well as the increase in energy density over time. Second, a thorough explanation of the structure and classification of MXenes is provided. The next section focuses on a thorough examination of several synthetic methods for individual MXene and MXene polymer composites. The general characteristics of individual MXene and MXene polymer composites are then specifically examined and summarized. The most recent developments in the electrochemical performance of MXene in diverse energy storage applications are then thoroughly covered. This paper aims to facilitate the continued development of MXenes and improved EST technology by addressing potential problems and prospects.

2. Overview of MXene

Two-dimensional (2D) materials have achieved significant popularity in recent decades due to their excellent qualities similar to 3D materials, as well as their intimate relationship with remarkable technical, commercial, and industrial applications. Such 2D materials include chalcogenides [25], transition metal dichalcogenides (TMDCs) [26], graphene [27], hexaboron nitrides (hBNs) [28], and doubled layered hydroxides [29]; they are examples of 2D materials that have piqued the curiosity of researchers in a wide range of fields [30]. Most materials have been thoroughly theoretically and practically investigated, particularly 2D materials with single-layer (SL) graphene and its extraction from exfoliated graphene [31,32]. As a result, numerous 2D materials (including tungsten disulfide (WS_2), hexagonal boron nitride (BN), and tungsten diselenide (WSe_2)) have been prepared by exfoliation. These materials are termed van der Waals (VdW) materials since there are few molecular interactions between the exfoliated layers [33]. In contrast, fabrication of SL-based 2D materials from layered 3D solids might be challenging due to intense bonding between the material interlayers (ILs).

After the development of graphene in 2011, the 2D substance known as MXene was discovered [34–36]. It is composed of carbide, nitride, or a combination of the two [34–36]. Exceptional characteristics of 2D MXene include high thermal and electrical conductivities as well as excellent oxidation resistance. The typical representational formula of this 2D material is $M_{n+1}AX_n$ (M stands for early transition metals, and n represents the number of layers, such as 0, 1, 2, or 3). To date, approximately 70+ MAX phases have been identified (Fig. 4a,b); shown are designations of the group III and IV-A elements, and X defines the nitrogen (N) or carbon (C) element or combination of both [37].

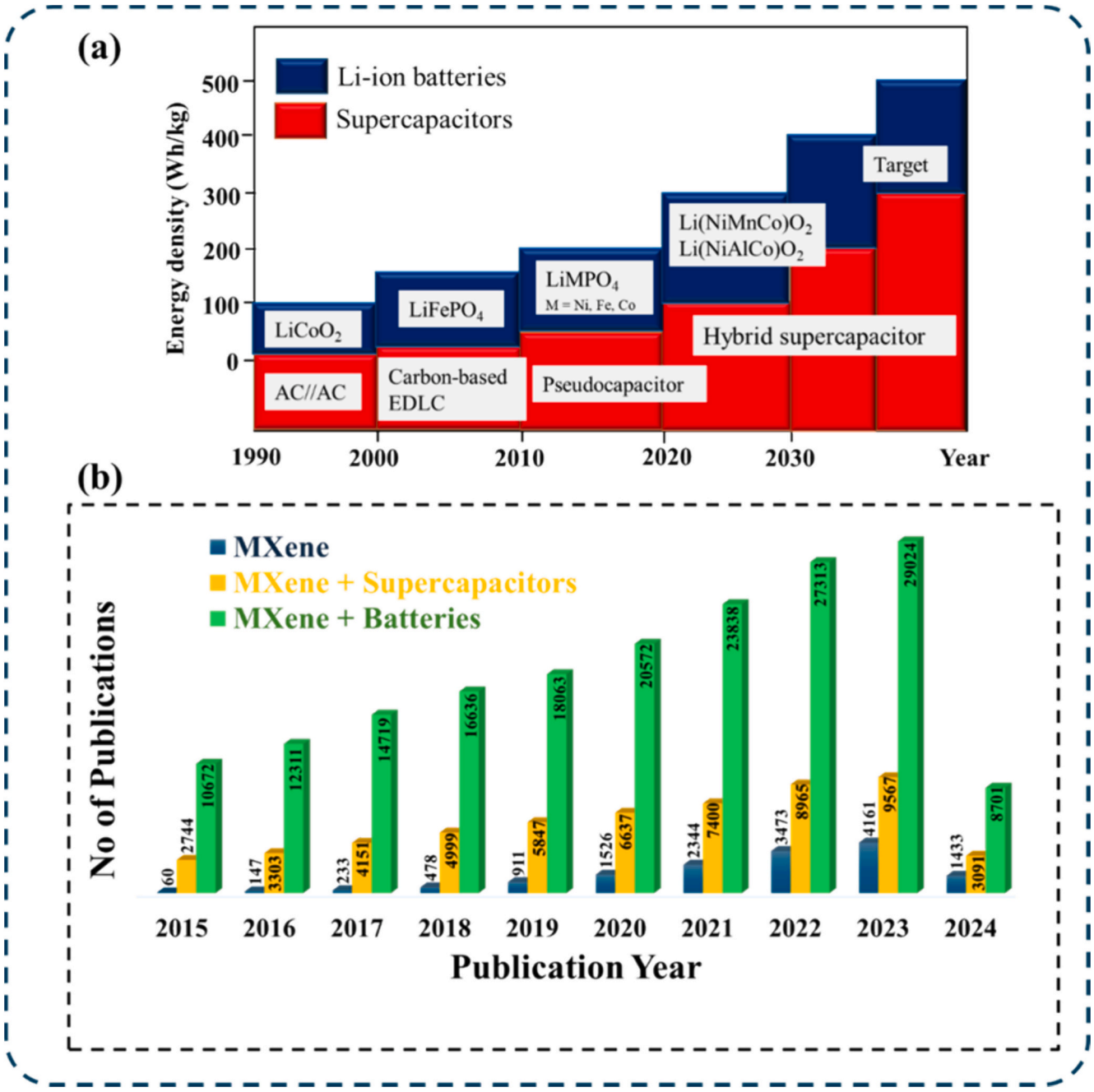

Fig. 3. a) Demanding performance of energy density performance for SCs and LIBs. b) Bar chart indicating the upsurge in journal publications focused on MXene materials for energy storage applications. The corresponding annual publications retrieved implementing "MXene", "energy storage", "MXene + supercapacitors" and "MXene + batteries" as a subject from 2015 to 2024 (database taken from Clarivate Web of Science).

Furthermore, the hexagonal structure of the MAX phase results in structural intergrowth based on the $M_{n+1}X_n$ layer, and A is the atomic sheet planar collecting along the c direction [38]. In general, MAX phases are the most stable and likely equivalent to the strongest bond IL formation between M–X, whereas the IL bond formation between A–A and M–A is considered to be the weakest, which contributes to layer A being more chemically reactive comparable with M-X in an environmentally favorable manner. This section discussed various MXene processing strategies, such as electrochemical, hydrothermal, direct and indirect, and microwave synthesis.

2.1. Electrochemical etching

Fabrication of MXene can be carried out by electrochemical etching, in which electrons are transferred from the "A" element to further precursor elements of the MAX phase. In this type of etching, the anode and cathode are separated, which causes a bias-induced etching mechanism to form the desired MXene. For this kind of etching, electrolytes such as hydrochloric acid (HCl), hydrogen fluoride (HF), and sodium chloride (NaCl) are commonly used. This method uses electrical currents to remove the A layers from the MAX phases selectively. It may be more environmentally friendly because it frequently calls for less corrosive solutions or can even be carried out in aquatic conditions. This has a lower environmental impact than standard chemical etching processes,

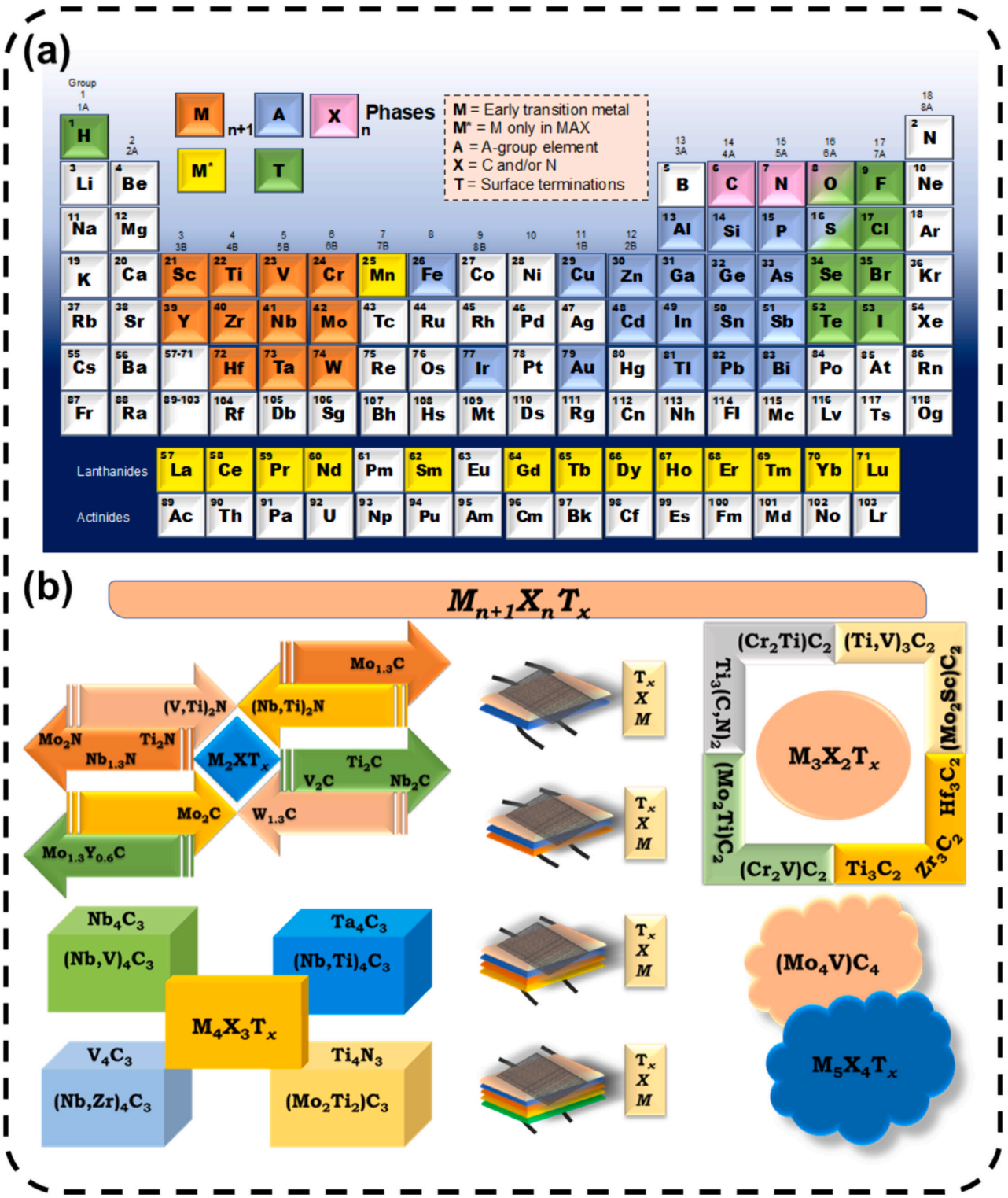

Fig. 4. a) Periodic table representing MXene layer formation in terms of surface termination, early transition elements, groups III and IV-A elements. b) MXene MAX phases are illustrated using the MXene formula in accordance with the number of layers.

which use highly corrosive acids. Electrochemical etching also allows for greater control over the etching process, resulting in more uniform and consistent layer removal. The first report to describe electrochemical etching of $Ti_3C_2T_x$ MXene in dilute HCl is by Sun, Shah [39]. Fig. 5a,b shows the X-ray diffraction (XRD) pattern and Raman spectra of the prepared material (which indicates that for XRD no such observable impurities in the parent Ti_2AlC MAX phase were evident) and the Ti/Al atomic ratio, respectively. The Raman pattern indicates that the vibrations of the Al atoms in MAX phase correspond to peaks at 275 and 350 cm^{-1}. This is because of contamination from the chamber, resulting in exaggerated C and O contents, as is normal for energy-dispersive X-ray spectroscopy (EDX) data reported by this group. Because of excessive etching, this method might remove the A and M layers and create carbide-derived carbons (CDCs). The HCl electrolyte

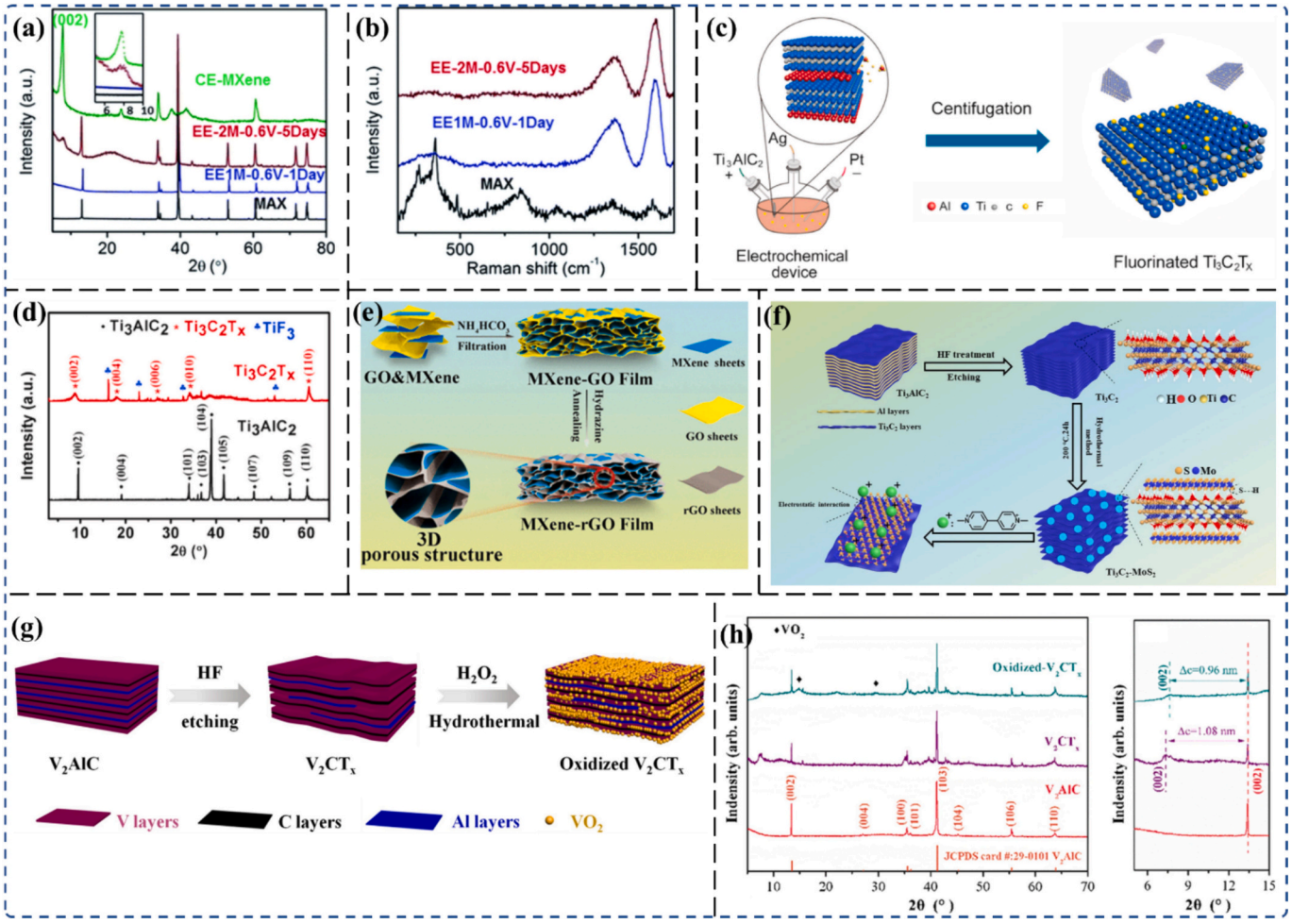

Fig. 5. a–b) XRD pattern and Raman spectrum of the as-synthesized MXene material. [39] c–d) Schematic for fabricating fluorinated MXene and XRD spectra of the bulk Ti_3AlC_2 MAX phase and formed $Ti_3C_2FF_x$ sheets. [40] e) Schematic for fabricating MXene with rGO by utilizing electrochemical etching. [41] f) Fabrication of MXene with MoS_2 by applying the hydrothermal method with freeze-drying. [42] g–h) Schematic of MXene preparation by hydrothermal processing and XRD spectra of the prepared material, representing the peak shift at certain directions. [43]

used in this process facilitates easy removal of Al from Ti_2CT_x MXene during electrochemical production of MXene from the MAX phase, in which MAX phase is the working electrode in a three-electrode configuration system. Moreover, continuous etching causes the CDC MXene and outer layer MXene to change into the inner MAX core. Thus, an original core–shell, three-layered structure is generated: consisting of the average MXene layer; outside CDC structure; and the inner, unetched core of MXene. Sonication may result in the separation of MXene layers from three-layered structures. This also confirms that it is difficult to avoid creating CDCs during etching.

Yang, Zhang [44] reported anodic corrosion of $Ti_3C_2T_x$ (T_x = O, OH) MXene in a binary aqueous electrolyte of 1 M ammonium chloride (NH_4Cl) and 0.2 M tetramethylammonium hydroxide (TMAOH, pH > 9). A binary aqueous electrolyte solution was used to prevent etching from proceeding solely on the surface, enabling the ions to enter the MXene layers maximally. The binary aqueous electrolyte and the MAX phase via a fluorine-free technique were used as the positive and negative electrodes in two-electrode assembly. Furthermore, the negative electrode actively engaged in the etching mechanism to enable Al-etching by preventing formation of the Ti—Al bond through the Cl ions from the electrolyte. On the other side, the only element engaged in the etching reactions was the anode, which enabled the etching of Al by rupturing the Ti—Al bonds with the facilitation of chlorine ions from the electrolyte. As a result, the layers are further intercalated by ammonium hydroxide (NH_4OH) ions, which also facilitates etching by expanding the etched anode edges. Additionally, there was no reaction on the positive electrode, which was used as the counter electrode. In addition, compared with the acid in fluorine etching, creation of MXene by this method results in superior electrical conductivity. This method results in 90 % yield, which indicates its viability as a method for fabricating MXene.

Yin, Li [40] reported the same methodology via controllable fluorination of MXene for battery applications. Initially, the ionic liquid electrolyte methyl cyanide (MeCN) and 1-butyl-3-methylimidazolium hexafluorophosphate ([BMIM][PF_6])—at ambient temperature—undergoes nonaqueous etching in a manner that avoids MXene oxidation during fabrication. In addition, the prepared material was completely fluorinated with titanium (III) fluoride (TiF_3) and CF in a manner that further electrochemically increased the cyclic performance of the MXene in LIB applications (Fig. 5c). Moreover, the XRD pattern in Fig. 5d shows the peak formation of the synthesized $Ti_3C_2F_x$ and Ti_3AlC_2, in which the (002) and (004) crystalline diffraction peaks were evident at 9.5° and 39°, respectively, for the MAX phase. A similar observation was made after exfoliation, in which the formed $Ti_3C_2F_x$ yielded a lattice parameter of 8.7° at peak (002), thus confirming the as-prepared material's tremendous electrochemical performance.

Ma, Zhou [41] formed an MXene composite with reduced graphene oxide (rGO) hybrid films by self-induced electrolyte harnessing for Li-ion energy storage. Fig. 5e shows the as-prepared MXene produced from the MAX phase by Al-layer etching using HF etchant. The

electrolyte used for this purpose was lithium hexafluorophosphate ($LiPF_6$), concomitant with ethylene carbonate and dimethyl carbonate. In addition, the fabricated composite films exhibited 30 % stability and a 335.5 mAh/g capacity at a current density of 4 A/g.

However, electrochemical etching also has certain drawbacks. Electrochemical setups can be complex and costly, requiring specialized equipment for precise application and management of electrical currents. This complexity may limit scalability, especially in large-scale industrial applications. Additionally, the electrochemical process parameters significantly influence the etching rate and quality of the resulting MXenes, necessitating meticulous adjustments for each type of MAX phase used. This variability can lead to incomplete etching of certain layers, resulting in MXene flake thickness and quality variations. Therefore, while electrochemical etching offers an environmentally friendly and precise method for producing MXenes, it demands careful control of parameters and substantial upfront investment in equipment and process development.

2.2. Hydrothermal processing

Forming 2D nanomaterials using the hydrothermal method is a one-step process. Several variables—such as temperature, time, and pressure—can be optimized to produce the desired material. The precursor material is placed in a stainless-steel autoclave and then held in a furnace at ~200 °C and up to 10 bars for a brief period. Various morphologies—including nanorods, nanoflowers, nanowires, and nanobars—have been created using the hydrothermal approach [45]. Because of structural degradation and material oxidation in adverse environmental conditions, the preparation methods for MXene from hydrothermal processing are fascinating. The construction of carbon-free TiO_2 on the surface of MXene produced through hydrothermal synthesis has been closely examined [46–48]. However, controlling the MXene's crystallinity and phase purity is one of the main advantages since the hydrothermal method produces highly defined crystal structures by operating at high pressure and temperature. The synthesis of MXenes with reduced flaws and improved quality is also possible with this technique since the aqueous medium provides a consistent and regulated reaction environment. Additionally, MXene surfaces can be functionalized during synthesis using the hydrothermal technique, incorporating functionalities in a single step that improves the material's characteristics for certain applications.

According to Guo et al., [42] Ti_3C_2 MXene can be produced by freeze-drying by utilizing the Ti_3AlC_2 MAX phase and combining it with MoS_2 by a hydrothermal process in a manner that creates a composite (Fig. 5f). The material produced using this technique has a flower-like texture on the MXene surface after the Al layer has been entirely removed. However, when MoS_2 sheets were placed on Ti_3C_2 MXene, scanning electron microscopy (SEM) analysis indicated a cascading petal-like shape. As a result, compared with synthetic MXene, the surface area of the composite sample was increased with a fundamental chemical change. Furthermore, the Ti_3C_2/MoS_2 sample's surface area increased by 60.49 %, confirming that the hydrothermal method used to create it is pertinent to subsequent MXene composite adsorption.

Using the same approach, Luo, Liu [43] reported the synthesis of oxidized vanadium carbide (V_2CT_x) with vanadium(II) oxide (VO) for electrochemical optimization of anode-based Li-ion batteries (Fig. 5 g). The XRD patterns of oxidized-V_2CT_x, V_2AlC, and V_2CT_x indicate that after HF treatment, the (0 0 2) peak of V_2CT_x expanded and shifted downward to 7.37° compared with the diffraction peaks of V_2AlC, indicating that V_2AlC was etched in a manner that produced V_2CT_x. Furthermore, only a portion of the Al layers was removed, as evidenced by the fact that the diffraction peaks of (0 0 2) and (1 0 3) formed at 13.39° and 41.17° (respectively) from V_2AlC remained partially evident. Additionally, there were two new diffraction peaks for oxidized-V_2CT_x at 14.83° and 29.50°, which might be attributable to VO_2 (Fig. 5 h). Recently, Numan, Rafique [49] reported microwave-assisted hydrothermal synthesis for fabricating $Ti_3C_2T_x$ MXene from Ti_3AlC_2. Extraction of MXene from the MAX phase experimentally confirms the effectiveness of the preparation technique for rapid, environmentally sustainable, facile, large-scale manufacturing of MXene. He, Wang [50] reported Mo_2CT_x MXene to monitor the electrolyte effect for SCs assisted via the hydrothermal approach (Fig. 6a). Fig. 6b shows Mo_2Ga_2C XRD patterns by etching. The predominant diffraction peak in I-Mo_2CT_x was Mo_2Ga_2C, whereas Mo_2CT_x MXene only had a small peak. In this etchant, Mo_2CT_x MXene could not be etched. The primary diffraction peak in II-Mo_2CT_x was also Mo_2Ga_2C, but this etchant exhibited evidence of temperature and time impacts on the etching. The peak of Mo_2CT_x MXene was higher than I-Mo_2CT_x at 110 °C etched for 5 days. Since there were no differences between the samples etched at 110 °C for 5 or 6 days, the impact of additional time on the etching result was minimal. The peak of Mo_2CT_x MXene increased in intensity compared with other conditions in II-Mo_2CT_x, after the Mo_2Ga_2C was etched at 120 °C for 5 days. As a result, the temperature substantially impacted the etching effect, with 120 °C being the ideal temperature. Moreover, the HF concentration was developed considering these findings in which the major phase peak of III-Mo_2CT_x shifted from Mo_2Ga_2C to Mo_2CT_x MXene; this new peak exhibited an intense diffraction peak. As a result, Mo_2CT_x MXene might be etched under III-Mo_2CT_x conditions. Therefore, the XRD pattern in Fig. 6b focuses on the lattice parameter 2θ range of 5–12° is also shown. Accordingly, the III-Mo_2CT_x was the best etching method, and the (0002) peaks for the Mo_2CT_x MXene might be used to estimate the c lattice parameter of the Mo_2CT_x MXene peak: i.e., 20.75.

Similarly, Wang, Shou [51] reported HCl-related hydrothermal etching fabrication of Mo_2Ga_2C MXene, which was initially Mo_2Ga_2C prepared through two-stage vacuum sintering (Fig. 6c). In accordance with the XRD spectra in Fig. 6d, the primary peaks were evident at (002), (100), (103), (008), (105), (107), (108), and (110); their corresponding lattice parameters (2θ) were positioned at 9.89°, 34.18°, 37.4°, 39.94°, 42.58°, 49.52°, and 53.5°, respectively. In addition, excessive etching can also cause carbides to develop (signal at 25°). Concentrated HCl can prevent oxidation during the etching, whereas lower reaction temperatures or dilute HCl decrease the effectiveness and quality, including oxidation of the finished product, even though there is less pressure. However, the hydrothermal approach has limitations. The need for high-pressure and high-temperature conditions demands the installation of specialized, durable equipment, which can raise the overall cost of the synthesis process. Additionally, scaling up hydrothermal synthesis can be difficult since maintaining constant conditions across bigger volumes is tricky and can result in discrepancies in the quality of MXene produced. Furthermore, the procedure is time-consuming compared to alternative technologies, such as microwave synthesis, which may limit its efficiency for large-scale manufacturing. Because of this, the hydrothermal technique has higher operating complexity and expense, even if it gives exact control over material properties.

2.3. Direct and indirect HF etching of MXene

Direct etching and indirect etching are two common methods for synthesizing MXenes, each with its own advantages and downsides. Direct etching eliminates A layers from MAX phases with powerful chemical etchants like hydrofluoric acid. This highly efficient process allows for the rapid and complete removal of A layers, yielding high-quality MXene with few remaining phases. This technique is simple and easily scaled up for large-scale production, making it a preferred alternative for commercially producing MXene. In contrast, indirect etching takes a gentler method, often employing less abrasive chemicals such as fluoride salts mixed with acids at high temperatures [52]. While this approach is slower and less efficient than direct etching, it is safer and more ecologically friendly, lowering the risks associated with handling extremely corrosive compounds such as hydrofluoric acid. Indirect etching also provides more control over the etching process, potentially resulting in MXenes with unique surface functions that

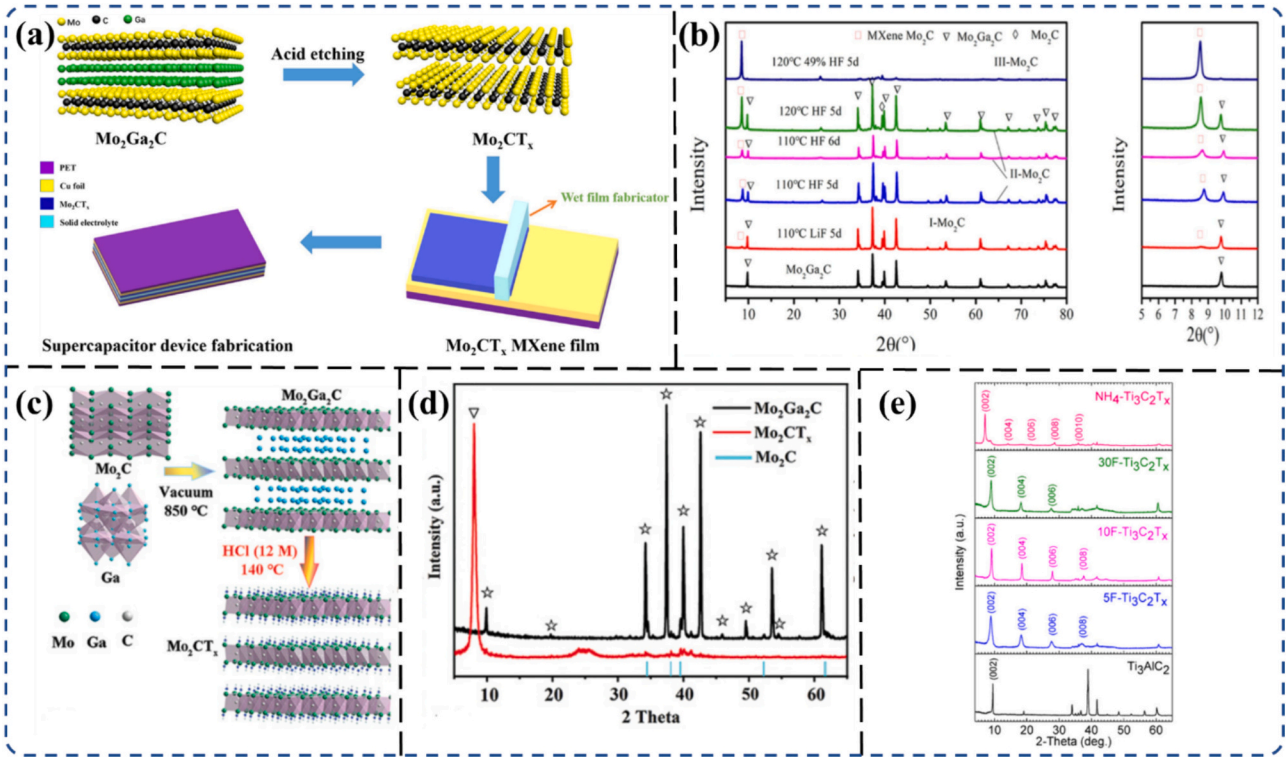

Fig. 6. a–b) Schematic of synthesized MXene for supercapacitor applications and XRD spectra of the as-fabricated sample in various etched conditions [50]. c–d) Schematic of MXene fabrication from the MAX phase and XRD pattern of the MAX phase as well as etched MXene [51]. e) XRD pattern of F–$Ti_3C_2T_x$ and NH_4–$Ti_3C_2T_x$ [60].

would not be possible with direct etching.

The most frequently used method for preparing MXenes was described for the first time by Naguib et al., [53], who etched Ti_3AlC_2 in 50 % HF for 2 h at room temperature. Using HF results in Ti—C ILs that are close to each other; thus, mechanical [54] or chemical [e.g., isopropylamine, water, dimethylsulfoxide (DMSO), hydrazine, tetrabutylammonium hydroxide, or urea] intercalation is required to insert substances with a large radius (e.g., –OH or H_2O) into the framework of the Ti—C by hydrogen bonding, and then expand the IL spacing of $Ti_3C_2T_x$ by sonication [55,56]. In this phase, the Al layer is etched by the powerful etching action of HF, along with some nearby Ti and C atoms, creating unstable and reactive Ti single vacancies or vacancy clusters that can decrease the size and provide sites for other metal salts [57,58]. The HF technique has been used to synthesis a variety of MXenes, including $Nb_{4/3}CT_x$, $Hf_3C_2T_x$, $Mo_2TiC_2T_x$, V_2CT_x, Ti_2CT_x, and Ti_3 [59–61]. Moreover, depending on the concentration of HF, the etching time varied from 2 to 165 h. A longer time is needed for lower HF concentrations. To date, 50 % HF is the ideal concentration for fully etching Al and producing homogenous MXene. All known MAX phases have a hexagonal close-packed (hcp) arrangement of the M atoms, with the X atoms in the octahedral interstices. MXenes layers maintain this arrangement but reduce the basal planes and increase the d-spacing lattice. In addition, Fig. 6e [61] shows the XRD pattern of F–$Ti_3C_2T_x$ produced by HF etchant by taking the different mass compositions at (5, 10, and 30 wt%); NH_4–$Ti_3C_2T_x$ prepared via ammonium bifluoride (NH_4HF_2) exhibited a considerable shift in the (002) peak which, corresponds to the 2θ lattice parameter at ca. 8.5 compared with that of MAX phase (Ti_3AlC_2). This occurs because of the lack of the peak at 39°, causing Al removal and insertion of T_x = F, —O, and –OH groups. The speed of MXene manufacturing could be increased via single molten etching rather than the comparatively slower HF technique. For instance, Urbankowski, Anasori [62] were the first to create multilayered $Ti_4N_3T_x$ in only 0.5 h by etching its precursor Ti_4AlN_3 powder at a relatively high temperature of 550 °C under flowing argon and molten fluoride salts (i.e., potassium fluoride (KF), lithium fluoride (LiF), and sodium fluoride (NaF)).

Other moderate and environmentally acceptable etchings—such as (NH_4HF_2), or acids [such as HCl and sulfuric acid (H_2SO_4)] with fluorine-containing metals or metal fluorides—could be utilized for manufacturing MXenes to avoid utilizing HF [e.g., LiF, NaF, KF, calcium fluoride (CaF_2), iron(III) fluoride (FeF_3), and cesium fluoride (CsF)] [63]. This enables subsequent etching of the "A" element as well as the interaction of both cations (NH^{4+} and Li^+) and H_2O into the layered structure of MXene; in a manner that produces more exfoliated MXene with a longer IL spacing, more minor defects, higher oxygen content (ca. 1.5×), better electronegativity of fluorine (ca. 3.5×), hydroxyl (ca. 2.0×), and higher stability than HF-etched MXene [64,65]. The two key components of indirect HF technique are the etching time and etchant concentration. Various MXenes [including Mo_2CT_x, Ti_3CNT_x, $Ti_3C_2T_x$, and $(Nb_{0.8}Zr_{0.2})_4C_3T$] have been generated by LiF (0.6–5 g) and HCl (6–12 M) etchants. However, 1 M NH_4HF_2 generated $Ti_3C_2T_x$ in only 12 h, whereas the other side LiF/HCl typically requires 12–384 h to enable etching of the A element in the MAX phase [65]. Sonication (i.e., probe sonication and water bath) can regulate the MXene flake size and IL spacing by direct HF as well as indirect etching [66]. Because probe sonication facilitates direct transfer of ultrasonic energy to MXene through the comparatively small circular cross section of the sonication tip, it exhibits higher irradiation power and creates smaller flake sizes during MXene delamination than water bath sonication [67,68]. To avoid MXene oxidation in water solution under air, the sonication should be carried out in an ice bath or under argon [68]. However, direct etching has certain drawbacks, too, such as the substantial safety concerns and environmental problems brought on by using extremely hazardous and corrosive chemicals that call for careful handling and disposal procedures. These elements may raise the complexity and cost of operations. Even while indirect etching is safer, it usually yields a lesser quality product and may need additional purification and processing processes to reach the same level of MXene purity and quality as

direct etching. Consequently, the decision between direct and indirect etching methods is based on the particular needs of the MXene application, the production volume, and safety and environmental factors.

2.4. Microwave synthesis of MXene

Microwave synthesis processing of MXene has also received much attention due to its ease of fabrication, which makes it easier to delaminate the MXene sheets during the synthesis and confirms this technique's efficiency for eco-friendly, rapid manufacturing, and large-scale development of MXene. The high-energy waves created by microwave irradiation can quickly and evenly heat the reaction mixture, producing MXene flakes with a more consistent quality. Additionally, this approach may precisely control the synthesis conditions, leading to improved control over the material's characteristics and possibly larger yields of the desired MXene. Zhu, Zhang [69] a scalable microwave heating-based method for creating MXene. The experiment involved combining equal amounts of HCl and LiF etchant, placing the mixture in a microwave oven, and irradiating it for 15 min at 200 W power. During the irradiation, the system exhibited bubbling due to the reaction of H^+ from HCl with the aluminum-based atom layer, leading to the production of H_2 gas. The etching process is predominantly initiated at the sidewalls of the bulk Ti_3AlC_2 phase. Upon completion of the process, MXene flakes were obtained after the sequential removal of —F, —Cl, –OH, and —O groups, respectively. Similarly, The application of MXene with polyionic liquid (PIL) for the adsorptive removal of iodine was reported by Sun, Sha [70]. The synthesized material produced by the microwave irradiation approach had an adsorption capacity of 170 mg/g, significantly higher than other adsorbents and unmodified MXene. Additionally, the manufactured material used in this process made it possible to remove adsorptive iodine individually and economically.

Recently, Using HCl/LiF, Numan, Rafique [49] used a similar technique to extract the MAX phase from Ti3AlC2. The elemental EDS analysis of the microwave-etched MXene shows that aluminum (Al) was hardly present and that the elements copper (Cu), carbon (C), oxygen (O), titanium (Ti), chlorine (Cl), and fluorine (F) are present. Moreover, the EDS analysis shows that all O, C, Ti, Cl, and F on MXene have a constant spatial distribution and that Al is always present freely. This indicates that the Ti_3AlC_2 MAX phase fully converts to $Ti_3C_2T_x$ following the effective delamination and etching process [72]. To explain the formation of delaminated $Ti_3C_2T_x$ MXene sheets and the timely etching of Al from the MAX phase using a microwave, it was also necessary to study the XRD spectra of the MAX phase and synthesize MXene. Following the successful treatment, the sharp peaks from the Ti_3AlC_2 sample that showed at 20°, 34.1°, 36.8°, and 41.9° nearly disappeared. The (002) peak of the precursor MAX phase migrated to a lower angle at 6.2° after being etched in the microwave, and a broad peak emerged at 6.2°, indicating the successful production of Ti_3C_2, respectively. According to [73], MXene from the MAX phase was microwave-synthesized by efficiently heating a mixture of Al, C, and Ti at 1300 °C for 30 min in a microwave oven. LiF (1.6 g) with HCl exhibits the maximum delamination degree in created MXene, the 1.35 nm interlayer spacing, and the 80 nm lateral size, respectively. This group synthesized the MXene by taking two etchant concentrations. The optical characterization of the produced MXene from the MAX phase resulted in 72 %–94 % transparency and sheet resistance of approximately 23,660 Ω $sq.^{-1}$.

In addition to the synthesis of MXene using microwave methods, which offers certain advantages, this approach also presents drawbacks. For instance, if rapid heating is not precisely controlled, it can lead to an uneven distribution of terminal groups on the MXene surface, potentially affecting the material's homogeneity and overall performance. Moreover, transitioning microwave synthesis from the laboratory to an industrial scale poses energy consumption and equipment design challenges. Microwave reactors must be specially designed to accommodate larger volumes while meeting stringent safety and energy efficiency requirements.

3. MXene/polymer-based materials

MXene and polymer-based composites are typically described as bulk materials used as fillers or components in which both ingredients are evenly disseminated. These materials are often aerogels or sponges comprised of MXene/polymer [74,75], MXene/polymer-coated polymeric textiles or fibers [76,77] and laminated composite materials and structure [78,79]. In-situ polymerization, hot or dry pressing, emulsion mixing, and solution blending are among the methods used to create MXene and polymer-based composites. However, solution blending is the most frequently used approach for synthesizing MXene and polymer materials. This section covers the many methods for creating composites using MXene and polymers.

3.1. Solution blending

Solution blending offers advantages for incorporating MXenes into polymer composites. MXenes' hydrophilic surface chemistry provides innate compatibility in polar solvents, enabling homogeneous dispersion throughout polymer matrices via solution mixing. This allows for control over composite morphology at the nanoscale, with MXene nanosheets or nanoparticles integrated uniformly within the host material. Compatible solvent selection also facilitates adjustments to component ratios during fabrication. The solution blending approach simplifies composite processing while achieving well-distributed, intimately mixed MXene-polymer nanocomposites. This enhanced interfacial contact and minimized agglomeration may optimize load transfer and phase interactions [80,81]. Typically, the MXene dispersion in a suitable polar dispersant (such as water [82], DMSO [83], and dimethylacetamide [83]) is compatible with the standard solution bending approach. Additionally, the dispersant can facilitate dissolution of the polymer, facilitating combination of the two substances in the same dispersant. To create the desired MXene/polyacrylamide (PAM) nanocomposite, Naguib, Saito [84] first dispersed MXene with DMSO and then dissolved this mixture in PAM with H_2O. However, this method is unreliable for obtaining a homogenous MXene/polymer composite dispersion at the molecular level. Similarly, MXene with long-chain cationic bromide enhances the surface and dispersibility in dimethylformamide (DMF), according to Si et al., [85] which confirms that the surface modification and dispersity in the polymeric matrix are improved by increasing the MXene dispersion in polystyrene. The XRD pattern in Fig. 7a indicates the presence of the ionic long chain modifier and the improvement of the IL distance within an etched MXene nanosheet. The IL distance/length of the alkyl chains participating in the cationic modifiers was both greatly increased after the MXene nanosheet was entirely etched and modified with di-hexadecyl dimethyl ammonium bromide (DDAB), octadecyl-trimethylammonium bromide (OTAB), and decyl-trimethylammonium bromide (DTAB). Fig. 7b shows thermogravimetric analysis (TGA) curves for Ti_3C_2, Ti_3AlC_2, exfoliated Ti_3C_2, DTAB–Ti_3C_2, OTAB–Ti_3C_2, and DDAB–Ti_3C_2. Between the ambient temperature and 700 °C, Ti_3AlC_2 was thermally stable under nitrogen without losing any mass. The mass of Ti_3AlC_2 gradually increased over the high-temperature range (ca. 500 °C to 700 °C), which is caused by selective oxidation of Al in Ti_3AlC_2 during heating under N_2 with a low oxygen concentration. To enhance the MXene dispersion in thermoplastic polyurethanes (TPUs), Yu, Tawiah [86] reported MXene surface modification with CTAB. CTAB, with the long alkyl chain over the MXene surface, generated a strong connection with the TPU matrix to aid in the dispersion; the produced nanosheets were used as a flame retardant for TPU (Fig. 7c). The XRD pattern in Fig. 7d indicates sharp peaks at 2° and 39°, corresponding to the characteristic peak at (104) of Ti_3AlC_2, which essentially was no longer evident after etching in LiF and concentrated HCl; confirming that Al was removed from the MAX phase. The (002) peak also changed to a lower 2θ lattice parameter, indicating

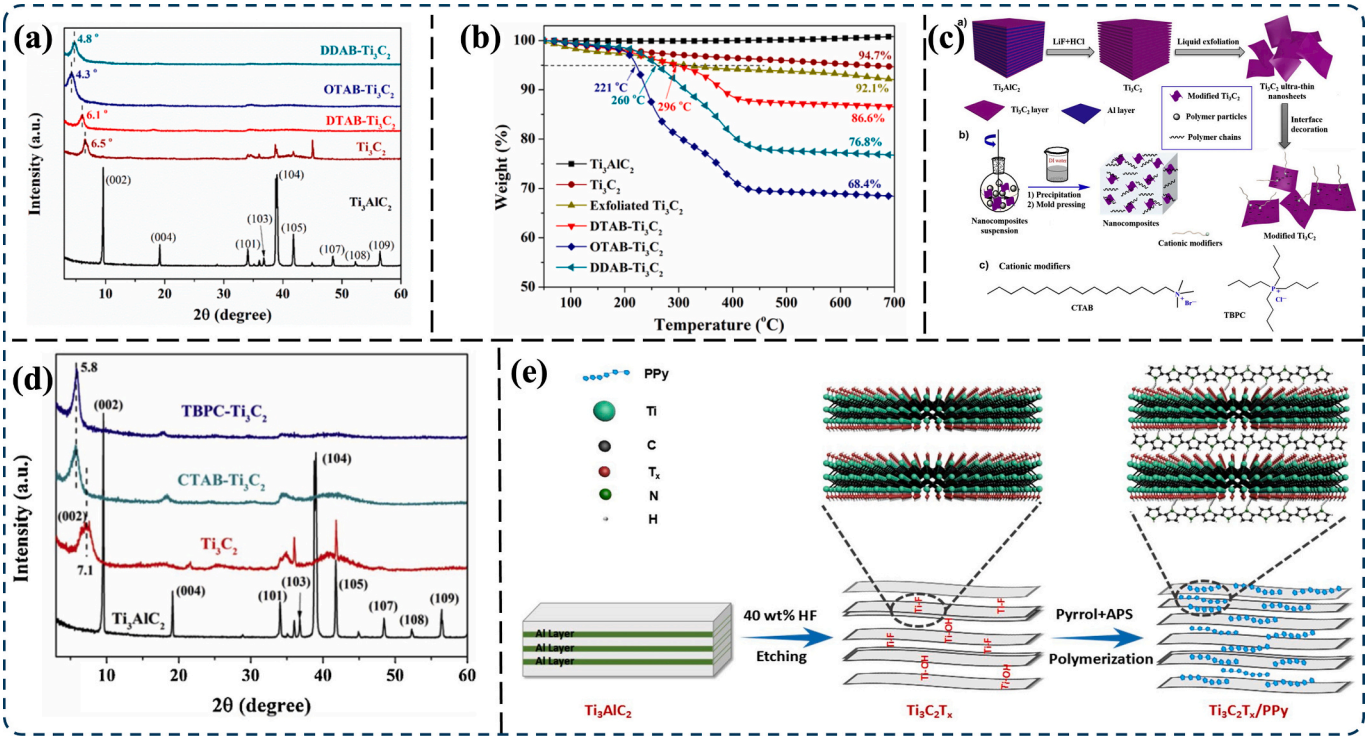

Fig. 7. a–b) XRD patterns of Ti_3AlC_2 MAX phase, Ti_3C_2, DTAB–Ti_3C_2, OTAB–Ti_3C_2, and DDAB–Ti_3C_2; TGA curves of Ti_3AlC_2, Ti_3C_2, exfoliated Ti_3C_2, DTAB–Ti_3C_2, OTAB–Ti_3C_2, and DDAB-Ti_3C_2 [85]. c–d) Schematic for fabricating MXene with CTAB and XRD characterization curves of the MAX phase and etched materials after solution blending [86]. e) Schematic for synthesizing $Ti_3C_2T_x$/PPy hybrids [89].

a longer IL distance in the etched Ti_3C_2 MXene [87]. A similar result was evident following modification of Ti_3C_2 by CTAB (after exfoliation) and TBPC (after delamination). Pan, Zheng [88] reported the same technique for synthesizing MXene–polymer based nanocomposites. They used a small quantity of $Ti_3C_2T_x$ dispersed in a poly (ethylene oxide)/lithium bis(trifluoromethanesulfonyl)imide complex (PEO_{20}–LiTFSI) to prepare MXene-based CPEs (MCPEs) for lithium metal batteries. Due to its hydrophilic surface, MXene was well-dispersed in the polymer matrix, as indicated by surface characterization respectively.

3.2. *In situ polymerization blending*

The wet method of in situ polymerization blending involves thoroughly mixing tiny molecules such as monomers, initiators, or curing agents with the MXene nanosheets. Organic particles are subsequently in situ polymerized into macromolecules, resulting in even dispersion of MXene throughout the polymer hosts. However, blending can greatly enhance the MXene dispersion in the polymer matrix. Production of MXene-containing polymer nanocomposites often uses this form of blending. The polymers used in the composites are thermosetting polymers, polymers with cyclic or heterocyclic units, or linear macromolecules that can polymerize under mild conditions [89–93]. Wang, Chen [94] reported in situ blending of $Ti_3C_2T_x$/epoxy resin nanocomposites. Preparing MXene/in situ polymerization polymer nanocomposites as electrodes, catalysis, shielding functional materials, and other purposes include polypyrrole (PPy), [92] polyaniline (PANI), [91] corresponding derivatives of both PPy and PANI, [90,95] polydopamine (PDA), [96] and other complex cyclopolymers; which can typically also be polymerized by in situ processing. By using in situ polymerization, Boota, Anasori [97] and Tong, He [89] created $Ti_3C_2T_x$/PPy composites (Fig. 7e). In situ polymerization blending substantially improved the electrical, thermal, and mechanical properties of polymers as well as the dispersion of MXene in the polymers, in addition to the interfacial adhesion between MXene and the polymer matrix. Moreover, Qin, Tao [92] reported a MXene/PPy nanocomposite with a 3D porous structure by in situ electrodeposition in pyrrole and MXene mixtures. For creating MXene-filled nanocomposites, certain linear polymers have also been polymerized in situ. MXene nanocomposites based on polyamide (PA) 6 were described by Carey, Hinton [93] by in situ ring-opening polymerization. To create relevant nanocomposites, linear polymers such as polyesters might be polymerized in situ; acrylic, olefinic, and polyamide precursor monomers are also accessible.

4. Properties of MXene/polymer hybrids

MXenes exhibit broad and adaptable surface interactions that are enabled by electrons and transition metal atoms. Many variables—such as the MAX phase material, etchant, and the procedure of etching and delaminating—substantially impact the surface chemistry, electrical, thermal, optical, magnetic, dielectric, and mechanical properties of MXene. The features of MXene can be modulated for suitable applications by altering its composition, such as by adding different “M” and “X” elements, as well as by altering the surface terminations. We present a summary of the main characteristics of MXene that relate to energy storage aspects; the aforementioned properties of MXene have been investigated recently from both experimental and theoretical perspectives [98]. Because of their improved mechanical strength, superior conductivity, and increased thermal characteristics, MXene and polymer materials exhibit substantial advantages. In this section, we highlight various properties related to MXene and polymer hybrids.

4.1. *Structural, compositional, functional, and surface properties*

The crystal structure of MXenes frequently adopts the P63/mmc hexagonal atomic lattice from their MAX precursor through selective etching, with the X atoms occupying the body center of the “M6X” octahedron. However, the type of etching techniques and the etching agents have the most substantial impact on the crystallinity and defects

of the MXene materials. Researchers have used many characterization methods, including SEM, EDX, Brunauer–Emmett–Teller (BET) techniques, XRD, and Raman spectroscopy. This section provides information on how to identify specific MXenes and validate the pathway of their production and fabrication using various analytical techniques. Ghazaly, Ahmed [99] demonstrated MXene synthesis by using local ultrafast (millisecond) Ti_3AlC_2 MAX phase to Ti_3C_2Tz MXene conversion, without applying an acid, by using surface acoustic waves (SAWs) in the presence of a low concentration of lithium fluoride (LiF, 0.05 M) (Fig. 8a). The Ti_3AlC_2 MAX phase (002) peak shifted from lattice parameter $2\theta = 9.5^\circ$ to 6° upon applying SAW, indicating a 4.5 expansion in the IL gap, "d" = c/2. This expansion is produced by the surface termination groups that replace the Al layer, as well as the intercalation of one layer of water and Li^+ ions. Scanning transmission electron microscopy (STEM) indicates single or multiple stacked layers with sheet widths up to 1 μm, demonstrating the material's 2D structure. Fig. 8b(i) indicates that the material was 2D. The long zones of consistent contrast represent single or numerous stacked layers with sheet diameters equal to 1 μm. Fig. 8b(ii) indicates local nanoscale particle agglomeration, evident as luminous regions in the image. The lattice-resolved structure from the same location is also evident, with the hcp structure of $Ti_3C_2T_z$ readily apparent. However, the structure also contains vacancies (dark spots) and vacancy clusters (dark irregular patches). Similarly, the lack of structure under the observed vacancies, even in small clusters of vacancies, indicates single-layer sheets. Fig. 8b(iii) is a higher magnification of the same image as Fig. 8b(ii), indicating individual atomic columns. Furthermore, the sheet had local surface terminations, as evidenced by the apparently sparsely close-packed luminous atoms across the sheet, given that the column intensity strongly depends on the local sheet alignment in reference to the electron beam.

Zhao, Zhu [100] used the sulfur-template strategy to construct 3D $Ti_3C_2T_x$ MXene foam, which exhibited good elasticity and can be used directly as a LIB anode. The (002) peaks of the porous $Ti_3C_2T_x$ MXene foams migrated to ca. 6.34°, corresponding to a 13.9 c-lattice parameter. The SEM results confirm that the MXene foam exhibited a high porosity architecture. The foam structure provided sufficient routes for electrolyte penetration, which is advantageous for electrochemical lithium storage. Fig. 8c indicates that changing the sulfur template percentage in the foam manufacture increased the number and size of the pores. The 3D MXene foam exhibited a porous structure, indicated by BET analysis, which might create a substantial number of active sites for lithium storage, facilitating inside access to the electrolytes and speeding up lithium-ion transfer.

Hu, Hu [101] evaluated the connectivity between two types of $Ti_3C_2T_x$ MXenes produced by etching the Ti_3AlC_2 precursor in aqueous HF (two solutions) over various concentrations (6–15 M/L) and then ultrasonically processing the resulting samples. Both the $Ti_3C_2T_x$-6 M and $Ti_3C_2T_x$-15 M electrodes were subjected to in situ electrochemical Raman spectroscopy measurements in H_2SO_4 to ascertain whether the surface functional groups were the source of the notable variance in electrochemical performance. At zero voltage, the Raman peak intensity of $Ti_3C_2O_2$ for the $Ti_3C_2T_x$-6 M electrode was higher than that for the $Ti_3C_2T_x$-15 M electrode, indicating that $Ti_3C_2T_x$-6 M exhibited more O terminations than $Ti_3C_2T_x$-15 M (Fig. 8d). Based on nitrogen adsorption–desorption studies, the specific surface areas (SSA) of the as-synthesized $Ti_3C_2T_x$-6 M and $Ti_3C_2T_x$-15 M were 3.5 and 40.5 m^2/g, respectively. However, substantial SSA frequently leads to large gravimetric capacitance for carbon-based materials, in which electrical double-layer capacitance (EDLC) predominates. Zhou, Zha [102] created a 2D hafnium containing $Hf_3C_2T_z$ MXene by selectively etching the Si alloyed AlC sublayer from the parent $Hf_3[Al(Si)]_4C_6$ MAX phase in concentrated HF. Notably, the etching caused the crystalline (003) peak of $Hf_3[Al(Si)]_4C_6$ to downshift, corresponding to an increase in the lattice parameter from 31.88 ($2\theta = 5.54^\circ$) to 32.70 ($2\theta = 5.40^\circ$). Additionally, the $Hf_3[Al(Si)]_4C_6$ secondary phase (003) peak widened and was somewhat displaced to a lower lattice parameter of $2\theta = 6.37^\circ$, indicating that $Hf_3[Al(Si)]_4C_6$ likewise underwent HF-induced transformation into Hf_2CT_z MXene.

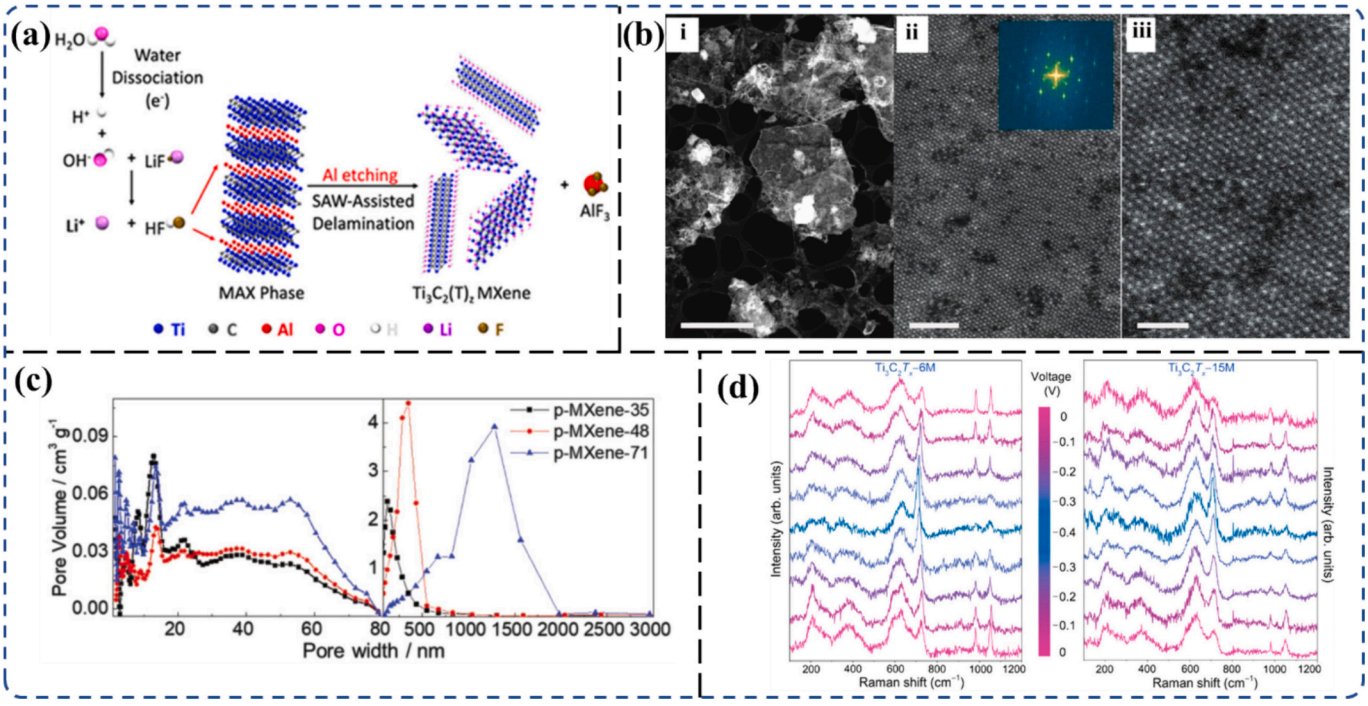

Fig. 8. a) Schematic for synthesizing $Ti_3C_2T_z$ MXene from the MAX phase through surface acoustic wave delamination with 0.05 M LiF [99]. b) HAADF–STEM images of the SAW-delaminated MXene; representing i) the layered structure of the uniformly thick MXene sheets, ii) local vacancies, and iii) separately resolved atomic columns. The scale bars are 2 μm, 2 nm, and 1 nm, respectively [99]. (c) Pore size distribution from the N-sorption and MIP results [100]. (d) In situ Raman spectra of MXene at 6 and 15 M [101].

4.2. Dielectric properties

The dielectric characteristics of materials have significance in supercapacitors and batteries due to their influence on the material's capacity for retaining electrical energy. The device's ability to store energy is increased when a material has a larger dielectric constant because it can hold more electric charge. In supercapacitors, where energy is kept by segregating charges at the interface of an electrode and an electrolyte, dielectric characteristics directly impact capacitance amount. The higher the value of the dielectric constant of the electrode material, the greater the capacitance, which corresponds to a greater amount of energy density [103–105]. Similarly, in batteries, dielectric qualities can influence the insulating properties as well as the effectiveness of charge separation processes within electrochemical cells, affecting both the battery's energy capacity and stability throughout charge cycles. Integrating materials with excellent dielectric characteristics can synergistically affect both supercapacitors and batteries, increasing their effectiveness, capability, and performance as a whole [104,106]. Combining these technologies is crucial in hybrid systems that combine the quick charging and discharging capabilities of supercapacitors with the enormous amount of energy of batteries, which leads to a balance of performance characteristics that outperform those provided by both technologies independently. Wang, Fan [107] studied the Ti_3AlC_2 composition and structure effects on $Ti_3C_2T_x$ MXene electromagnetic wave absorption. They etched five types of Ti_3AlC_2 MAX phases (TC1–TC5) with aqueous HF to produce $Ti_3C_2T_x$. Fig. 9a shows the complex permittivity (real/imaginary portions), tangent dielectric loss, and electrical conductivity of each $Ti_3C_2T_x$ sample. The average real and imaginary parts were 18.51 and 2.31 for TC1, 9.14 and 0.66 for TC2, 8.35 and 0.26 for TC3, 29.66 and 7.91 for TC4, and 10.62 and 0.69 for TC5. The $Ti_3C_2T_x$-based samples' various microstructures led to noticeable changes in their dielectric properties. Dielectric loss is of two forms: conductive and polarization loss. To further understand how the flake area and impurity content affected the dielectric characteristics, the electrical conductivity of the $Ti_3C_2T_x$-based samples was assessed for each sample. The electrical conductivities were 5.5×10^4, 3.8×10^4, 3.1×10^4, 1.41×0^3, and 3.8×10^4 S/m for TC1–TC5, respectively, in accordance with their complex permittivity. Xu, Wang [108] conducted an investigation into the effects of various solvents, including DMF (denoted as f-$Ti_3C_2T_x$), ethanol (mentioned as e-$Ti_3C_2T_x$), and DMSO (denoted as s-$Ti_3C_2T_x$), on the properties of $Ti_3C_2T_x$ MXene nanosheets during ultrasonication (Fig. 9b) [108]. The f-MXene yielded more-effective dielectric materials for electromagnetic wave absorption. Fig. 9c indicates that particularly between 2.0 and 12.9 GHz, f-Ti_3CT_x

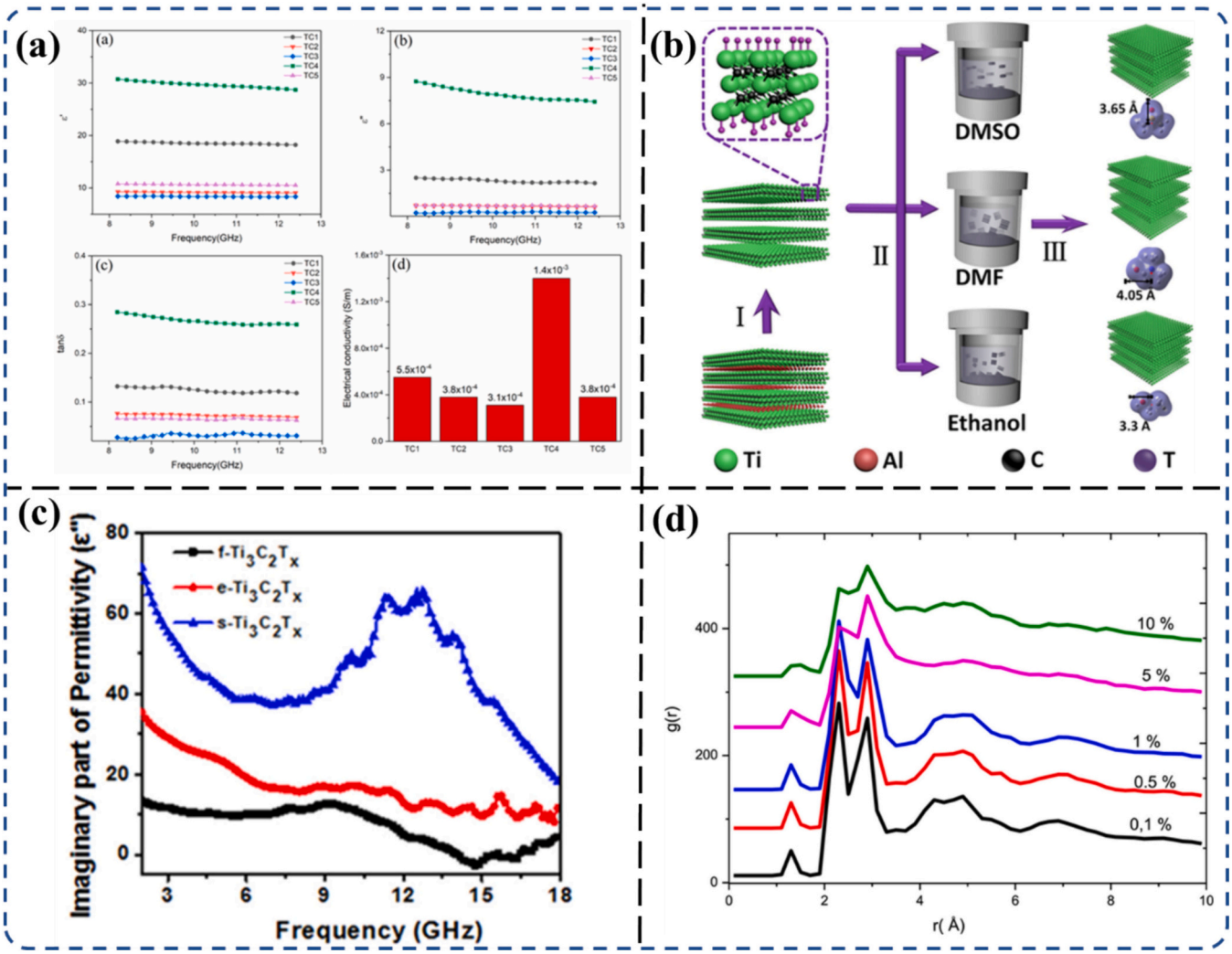

Fig. 9. a) Real part, imaginary part of the permittivity, tangent dielectric loss, and electrical conductivity for various $Ti_3C_2T_x$-based samples (TC1–TC5) [107]. b) Illustration of the ultrasonication–solvothermal technique used to create $Ti_3C_2T_x$ MXene nanosheets with characteristics that are determined by the solvent; using DMSO, DMF, and ethanol as the solvent. c) Imaginary (ε'') parts of the complex permittivity of *f*-$Ti_3C_2T_x$, *e*-$Ti_3C_2T_x$, and *s*-$Ti_3C_2T_x$ over the frequency range of 2.0–18.0 GHz [108]. (d) Radial distribution function of the 2D Ti_3C_2 with single-pore 38.642 $Å^2$ for various strains as a function of *r* [110].

exhibited a lower permittivity than either *e*-$Ti_3C_2T_x$ or *s*-$Ti_3C_2T_x$; indicating that dielectric loss was the main method used to absorb the energy of incoming EM waves (all three samples exhibited high ε'' values) [108]. Cui, Zheng [109] analyzed the 2D $Ti_3C_2T_x$ MXene EM wave absorption capability at frequencies ranging from 2 to 18 GHz. As the mass fraction increases from 25 wt% to 75 wt%, the values of ε' and ε'' increased as well. In contrast, for samples with a low MXene mass ratio, the ε' and ε'' values were quite steady at frequencies between 2 and 15 GHz, but at 15 GHz with a 55 wt% mass ratio. The values of the dielectric loss tangents (tanδ) exhibited an increasing trend in which increasingly convex peaks for tanδ were evident at 8.5, 12.4, 14.8, and 16 GHz. These tanδ values further indicate an increasing trend with increasing mass ratio. Additionally, the corresponding peaks were attributed to the dielectric loss (corresponding to the dielectric properties; the characteristics of which are greatly impacted by a material's electronic, ionic, space charge, Debye dipole, and interfacial polarization).

4.3. Mechanical properties

The mechanical characteristics of materials utilized in supercapacitors and batteries have significance because they drastically impact the durability, flexibility, and lifetime of these battery-powered devices. Excellent mechanical durability indicates that the electrodes can sustain physical loads and strains. The robust mechanical qualities of supercapacitors avoid structural failure at high charge and discharge rates, preserving the electrode materials' integrity [111]. Batteries, particularly those used in wearable and flexible electronics, must be able to withstand flexing and other deformations without losing functionality. Incorporating materials with better mechanical qualities can considerably improve the durability and lifetime of these devices, allowing them to be used in a wider variety of applications. Throughout production and running without deteriorating, which is essential to longevity. This combination of mechanical durability and electrochemical performance implies that both supercapacitors and batteries can function in harsh environments, expanding their practical applications and enhancing overall performance [112]. Enhanced mechanical features not only contribute to longer device lives but also help to progress new technologies like bendable and rollable electronics, where flexibility and durability are just as critical as electrical properties [113]. For 2D materials, owing to the strong covalent bonds between transition metals and other elements, MXenes' commercial applications—particularly for electrochemical energy storage—substantially depend on mechanical properties, such as flexibility [114]. Several theoretical studies have revealed that MXenes have better mechanical properties (e.g., Young's modulus, storage modulus, tensile strength, and fracture strain) than their corresponding MAX phases. The mechanical properties of MXenes are strongly influenced by their surface terminations. Accordingly, O-terminal MXenes are more elastically stiff than F/OH-terminal MXenes, [115] which is related to the lattice constant of the MXene that interacts with various terminals [116]. In addition, the number of atomic layers affects the mechanical properties of MXenes. $M_{n+1}X_nT_x$ becomes increasingly hard and strong upon decreasing *n*. Gounzari, Belkassmi [110] used a molecular dynamics simulation with a reactive force field (ReaxFF) potential to investigate the mechanical properties of 2D, nanoporous Ti_3C_2 MXene membranes. For nanoporous Ti_3C_2 (112 rectangular pores) with 28.666° 2θ and 38.639° 2θ, the projected fracture pressures at 300 K were 30.09 and 28.25 GPa, respectively, whereas Young's modulus was 475.699 and 421.008 GPa, respectively. Understanding the structural progression of samples under tensile strain is a crucial tool for investigating a material's fracture and mechanical behavior. Fig. 9d shows the progression of the radial distribution functions (RDFs) for various strains over time as a function of *r*. With increasing strain, the intensity of the second and third peaks—which indicate the medium and long-range order—substantially decreased. The monolayer lost its order at long and medium ranges because of sample breakage, which altered the atomic locations. Wide peaks [117] attributable to the alteration of the nanosheet structure because of the strain also indicate that the sample lost its order at the medium and long ranges because of the fracture. In addition, because of the many advantages of $Ti_3C_2T_x$ MXene is crucial for enhancing the mechanical properties of organic coatings. He, Cai [118] used spraying to make *k*-Ti_3C_2 composite coatings and used amination to make amino-grafted $Ti_3C_2T_x$ nanosheets. The mechanical and tribological features under challenging operating conditions have been thoroughly studied. Fig. 10a shows the storage modulus (E′) of coatings consisting of Ti_3C_2–0.75, *k*-Ti_3C_2–0.75, and a pure interpenetrating polymer network (IPN), indicating a material's capacity to retain elastic deformation energy and the stiffness of viscoelastic materials; E′ is an index used to gauge how well coating materials resist deformation [119]. E′ exhibited a notable improvement in Ti_3C_2–0.75 and *k*-Ti_3C_2–0.75 composite coatings from 40 °C to 120 °C, increasing by 110.52 %, in contrast to the pure IPN coating. In addition, the pure IPN coating exhibited the lowest storage modulus at room temperature (25 °C), but the *k*-Ti_3C_2–0.75 coating exhibited the highest (1860.09 MPa), indicating the longevity of the coating.

The mechanical performance of MXene and polymer-based composites is one of their most important features and can be substantially improved by adding inorganic fillers. Because of their unique characteristics, nanostructures, and reactivity, nanomaterials are appealing as fillers for strengthening MXene/polymer-based materials in a variety of polymers. The mechanical characteristics of the polymer materials—especially ultimate tensile strength (stress at materials breaking), yield strength (an elastic limit), Young's modulus (also rigidity; flexibility is its inverse), elongation at break (an index of materials toughness to some extent), and hardness—could be substantially improved with MXene. Cao, Chen [120] used the surface groups on $Ti_3C_2T_x$ to form hydrogen bonds with –OH groups on the surface of cellulose nanofibers (CNFs) and thus produce a $Ti_3C_2T_x$/CNF composite paper with superior mechanical qualities. Fig. 10b indicates that the tensile strength and fracture strain of the paper increased by 174.6 % (range from 49.3 MPa of pure CNF paper to 135.4 MPa) and similarly, 6.7 % (from 10 % of bare CNF paper to 16.7 %) after adding 50 wt% MXene respectively. As shown in Fig. 10c, the materials are tough and have a substantial Young's modulus; values of 135.4 ± 6.9 MPa, 16.7 ± 0.7 %, 14.8 ± 0.4 MJ/m^3, and 3.8 ± 0.3 GPa, respectively. However, the *d*-$Ti_3C_2T_x$/CNF composite paper (50 wt% *d*-$Ti_3C_2T_x$) can hold a mass of ca. 500 g without breaking. Therefore, the researchers noticed that strong interfacial adhesion, homogeneous dispersion, and chemical interactions between MXene and the macromolecules were key elements for increasing the strength and toughness of the MXene/polymer nanocomposites. Additionally, the MXene filler increased the polymer's crystallinity, increasing the overall strength of the composites. Zhou, Niu [121] indicated that Ti_3C_2 enhanced the mechanical characteristics of ultrahigh-molecular-weight polyethylene (UHMWPE) and reported that adding MXene caused the polymer tensile strength to increase nonlinearly. In addition, the friction resistance was improved, and the overall improvement effect was sufficiently substantial; the friction coefficient decreased from 0.186 of UHMWPE to 0.128 of Ti_3C_2/UHMWPE at 2 wt% Ti_3C_2. The composite ultimate tensile strength increased by 8.6 % as a result of adding 0.75 wt% Ti_3C_2, from 36.61 MPa of pristine UHMWPE to 39.65 MPa (Fig. 10d). Additionally, the minor improvement in the ultimate tensile strength in this situation might result from poor blending attributable to mechanical mixing and the fact that UHMWPE has a molecular weight that imparts difficulties in melting. Moreover, 2D MXene can increase the polymer elastic modulus, but it can also act synergistically with other fillers to further increase the polymer elastic modulus. For example, Xia, Mathis [122] used Ti_3C_2 nanosheets and cellulose nanocrystals (CNCs) to increase the mechanical strength of polyvinyl alcohol (PVA) nanofibers. They reported that the storage modulus of pure PVA nanofibers might be increased by 20 % by adding 0.14 wt% CNC. However, the storage modulus improved by >100 % and reached up to 855 MPa (after simply incorporating 0.07 wt

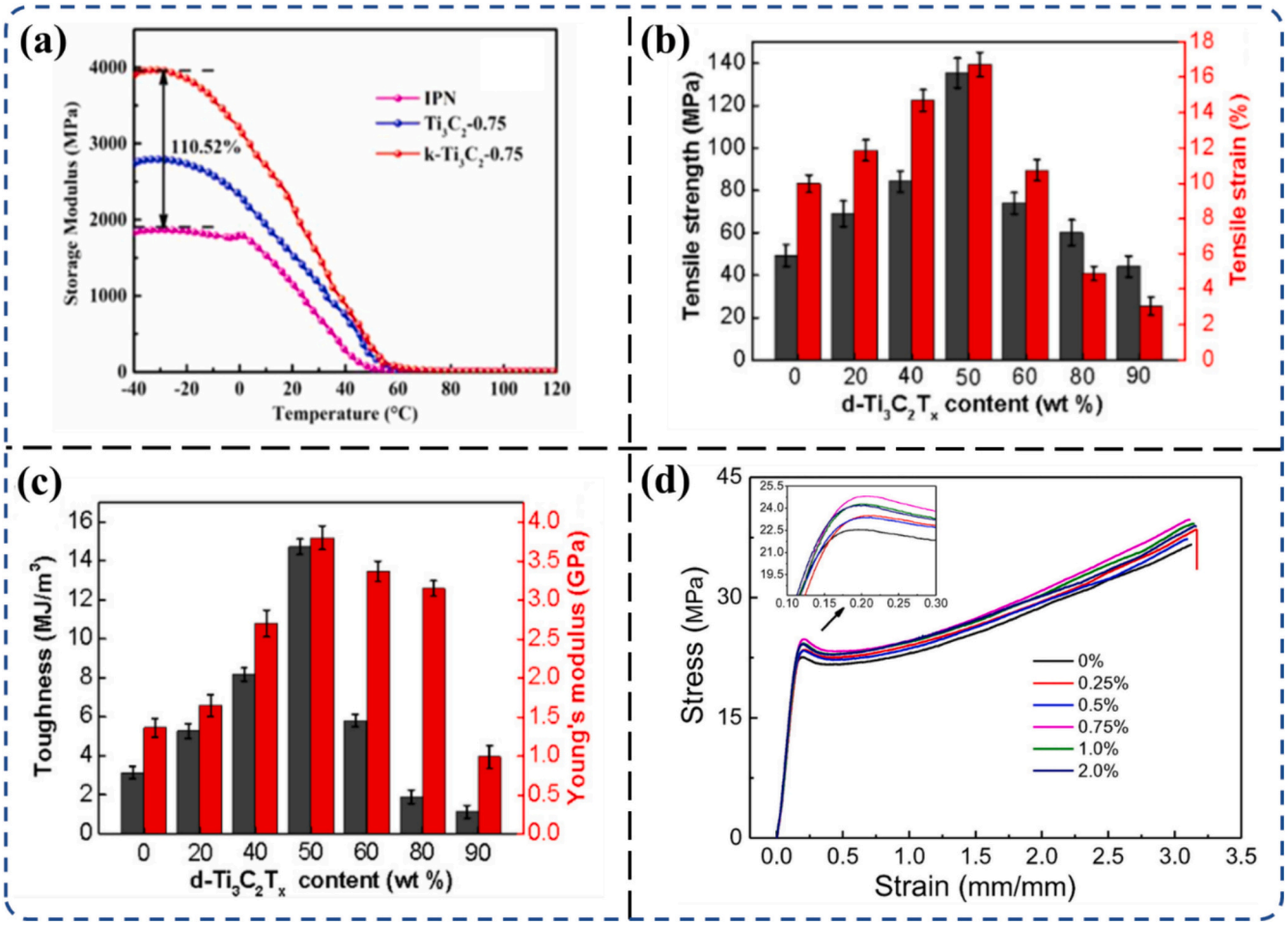

Fig. 10. a) Storage modulus vs. temperature of pure IPN, Ti_3C_2–0.75, and *k*-Ti_3C_2–0.75 coatings [118]. b–c) Tensile strengths and strains of the *d*-$Ti_3C_2T_x$/CNF composite paper with various *d*-$Ti_3C_2T_x$ contents, as well as toughness and Young's modulus of the d-$Ti_3C_2T_x$/CNF composite paper with various *d*-$Ti_3C_2T_x$ contents [120]. d) Stress versus strain graphs of Ti_3C_2/UHMWPE composites: inset, zoom-in of the curves of the yield phase [121].

% MXene nanosheets and 0.07 wt% CNC); substantially greater than that of pure PVA fiber (392 MPa).

4.4. Electrical properties

Like mechanical and dielectric properties, materials' electrical properties, notably their conductivity, are crucial to the operation of supercapacitors and batteries because they directly influence the efficiency and velocity of charge transfer. High electrical conductivity in electrode materials allows for quicker electron movement, which is critical for reaching enormous power densities in supercapacitors [123,124]. Supercapacitors can charge and discharge in seconds because of their quick electron transfer capabilities, making them perfect for applications requiring short power bursts [125]. In batteries, improved electrical conductivity reduces energy losses during both charging and discharging cycles, increasing total energy efficiency and allowing for more steady and sustained power production. Improved electrical characteristics of supercapacitors and batteries have a synergistic influence because they contribute to greater performance parameters such as enhanced lifespan, charge rate capabilities, and energy and power densities, respectively [126]. This synergy improves the efficacy of hybrid energy storage systems that combine supercapacitors' rapid charge-discharge properties with batteries' larger energy capacity, resulting in devices capable of delivering both high power and energy over long periods. Improved electrical characteristics improve individual device performance and broaden the spectrum of possible applications for these technologies in highly energy-intensive industries [127].

However, from the past few years, the impact of various M, X, and surface functions on the electrical characteristics of MXenes has recently been studied using integrated theoretical models. By changing the surface functional groups as well as the M functional groups, MXene electrical properties—including their conductivity and semiconductivity—can be optimized. Although some carbonitride with additional electrons can facilitate the band structure shift and facilitate metallic performance, carbides with surface termination consistently act as semiconductors in the class of MXenes. Whereas many monolayer MXenes with an O termination are semiconductors, monolayer MXenes without a termination are likely to be metallic [128,129]. For instance, Sunita, Ghanekar [130] used the computational tool Atomistic Tool Kit (ATK) to conduct density functional theory (DFT) calculations to examine the impact of surface functionalization on the electrical and optical properties of 2D V_3C_2 MXene. After examining their electronic band structures, all the heteroatoms (S, F, Cl, B, O, N, and Br) adsorbed V_3C_2 MXene-based semiconductors. B-, O-, and F-adsorbed V_3C_2 MXene structures exhibited a direct bandgap (0.50–1.26 eV); whereas N-, Cl-, and Br- adsorbed V_3C_2 MXene structures exhibited an indirect bandgap (0.80–1.19 eV). Both pristine V_3C_2 MXene and S-deposited V_3C_2 MXene exhibited metallic characteristics with a zero-energy band gap due to the conduction and valence bands intersecting at the Fermi energy level (Fig. 11a). Mostafaei and Abbasnejad [131] investigated the electrical and optical properties of M_2CT_2 (M = Y, Sc; and T = F, Cl) MXene monolayers using first-principles DFT computations. Semiconducting behavior was achieved in 2D monolayers of Sc_2CF_2, which exhibited an indirect band gap as follows: pristine, 1.06 eV; Sc_2CCl_2, 1.31 eV; Y_2CF_2,

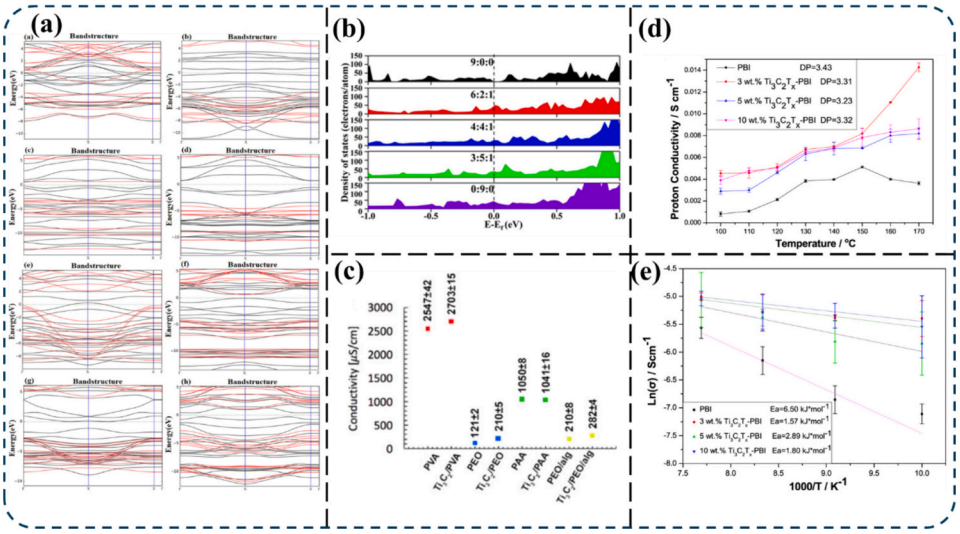

Fig. 11. a) Electronic band structure of pristine V_3C_2; and boron-, nitrogen-, sulfur-, oxygen-, fluorine-, chlorine-, and bromine-adsorbed V_3C_2 [130]. b) DOS of five MXene terminal ratios (T = O: F: OH): 9:0:0, 6:2:1, 4:4:1, 3:5:1, and 0:9:0 [132]. c) Conductivity plot of $Ti_3C_2T_x$/polymer solution [133]. d–e) Proton conductivities of PBI and $Ti_3C_2T_x$–PBI membranes, as well as Arrhenius plots of PBI and $Ti_3C_2T_x$–PBI membranes [134].

0.98 eV; and Y_2CCl_2, 0.69 eV. In addition, the electronic partial density of states (PDOS) for the monolayers of Y_2CCl_2, Sc_2CCl_2, Y_2CF_2, and Sc_2CF_2 indicates that most of the valence band close to the Fermi level consisted of C-*p* states, with only a slight overlap with the Sc-*d* or Y-*d* orbitals, indicating that the Sc—C or Y—C bonds are covalent in nature. Sc-*d* or Y-*d* states were more prevalent in the conduction band above the Fermi level. In this work, they also investigated the electronic structure, optical properties, photocatalytic activity, and quantum capacitance (QC) of Sc_2C and Sc_2CT_2 monolayers by using first-principles calculations.

Zhang, Chen [132] performed DFT simulations based on Vienna Ab initio Simulation Package (VASP) code to investigate the electronic properties of Na intercalation into five $Ti_3C_2T_x$ terminal ratios (T = O: F: OH): 9:0:0, 6:2:1, 4:4:1, 3:5:1, and 0:9:0. Fig. 11b indicates that the Ti-3*d* orbital primarily contributed to the high electronic conductivity of all MXene bilayer structures. Moreover, the $Ti_3C_2T_x$ MXene with O: F: OH = 6:2:1 exhibited superior conductivity than $Ti_3C_2O_2$ MXene, attributable to the presence of F that ensured the conductivity of Ti_3C_2–MXene. Similarly, by using VASP, Cui, Li [135] conducted first-principles simulations that evaluated the electronic/optical characteristics, photocatalytic activity, and quantum capacitance (QC) of monolayer Sc_2C and Sc_2CT_2 MXene. The electronic band structures further indicate that Sc_2CT_2 monolayers (T = P, Se, Si) exhibited metallic-like behavior. In the PDOS analysis, the conduction bands of Sc_2CT_2 (T = F, Br, OH, Cl, and O) monolayers were primarily obtained from Sc-*d* states, whereas the valence bands of Sc_2CT_2 (T = O, F, Br, Cl, and OH) monolayers were primarily derived from C-*p* and Sc-*d* states. In theoretical research, Chibani, Yahi [136] used DFT calculations to examine the structural, mechanical, and electrical properties of M4C3 MXene monolayers (M = Mo, Zr, Sc, Hf, Ti, and W). The Perdew–Burke–Ernzerhof (PBE), PBE + U, SCAN, and HSE06 approaches were used to assess the electronic exchange correlation energy. The spin-polarized band structures of 2D W_4C_3, Hf_4C_3, Sc_4C_3, Ti_4C_3, Mo_4C_3, and Zr_4C_3 MXene (which all exceeded the Fermi level) indicate metallic character in all the systems. Additionally, the M-*d* and C-2*p* orbitals of Ti_4C_3, Hf_4C_3, Zr_4C_3, and Sc_4C_3 MXenes hybridized with group III and IV M atoms in a manner that produced valence states below the Fermi level. The total density of states and PDOS were also calculated. Moreover, 2D MXene exhibits high electrical conductivity, close to that of graphene (9880 S/cm) [137,138]. As a result, MXene addition to polymer hosts might greatly enhance the conductivity of polymers. For instance, Mayerberger, Urbanek [133] reported that $Ti_3C_2T_x$/polyethylene oxide (PEO) nanocomposites had an electrical conductivity of 210 μS/cm; a 73.6 % increase compared with the PEO host (121 μS/cm) (Fig. 11c). The conductivity of the composite samples increased substantially, by many orders of magnitude (from the insulted condition of PAM to 3.3 S/cm), when Naguib, Saito [84] manufactured $Ti_3C_2T_x$/PAM nanocomposites (with only 1.7 vol% MXene). Moreover, the electrical conductivity of the composite depended on its MXene content and inherent electrical properties, and as the electrical conductivity of the MXene improved, that of the composites did as well. In addition to enhancing the composite's electronic conductivity, MXene also improved the system's ionic conductivity. Fei, Lin [134] created a composite membrane comprised of $Ti_3C_2T_x$ and polybenzimidazole (PBI). They reported that the membrane proton conductivity was >2× that of the PBI membrane. The researchers speculate that the following two reasons were responsible for the increase in proton conductivity of the composite membranes. One was that $Ti_3C_2T_x$ created linked ion channels and established long-range interfacial routes in the membrane due to its high aspect ratio (Fig. 11d). The other reason is that interactions between the polymers and the hydroxyl as well as oxy groups on the surface of $Ti_3C_2T_x$ led to an enrichment of the acid/base groups of the polymer matrix at the interface between the MXene and polymer. The composite membrane exhibited a high proton transfer rate and a low proton transport barrier due to both characteristics providing rapid proton migration sites. Moreover, the interactions between PA, PBI, and $Ti_3C_2T_x$ at the interface might be responsible for the increase in conductivity. Oxygen-containing groups on the $Ti_3C_2T_x$ surface might establish hydrogen bonds with $H_2PO_4^-$, and –NH provides additional protons with hopping sites. Fig. 11e shows the Arrhenius plot that was used to compute the membrane's ion transport activation energy (E_a), which is often used to evaluate the resistance to charge transfer [139]. The E_a of the PBI membrane was 6.5 kJ/mol, whereas the E_a values for composite membranes including 3 wt%, 5 wt%, and 10 wt% $Ti_3C_2T_x$ were 1.57, 2.89, and 1.8 kJ/mol, respectively. Since less activation energy is needed in composite membranes, proton transport should be simpler because E_a acts as an energy barrier for proton leaps between sites.

5. MXene for supercapacitors

MXene materials' remarkable electrical conductivity, hydrophilic surface, and superior mechanical qualities have made them extremely attractive supercapacitor electrode materials. High electron and ion transport rates are made possible by the structure of MXenes, which is

made up of transition metal carbides, nitrides, or carbonitrides. These rates are essential for the quick charge-discharge cycles found in supercapacitors. High surface area exposure is made possible by their two-dimensional layered architecture, which increases electrolyte accessibility and, hence, capacitance. [115] described a new high-yield approach to synthesize MXene that was simpler, safer, and offered a quicker way to produce delaminated MXene flakes. The material produced by this process resembles clay and may be rolled into thin sheets or sculpted to create conductive solids in a variety of shapes for a variety of uses. The rolled films performed exceptionally well as supercapacitor electrodes in an H_2SO_4 electrolyte, achieving volumetric capacitances of up to 900 F.cm^{-3} or 245 F/g' respectively. Lukatskaya, Mashtalir [140] revealed that cations from aqueous salt solutions may spontaneously intercalate between two-dimensional (2D) Ti_3C_2 MXene layers. A wide range of cations, including Na^+, K^+, NH^{4+}, Mg^{2+}, and Al^{3+}, may also be electrochemically intercalated, resulting in >300 F per cubic centimetre capacitances. This work establishes a foundation for investigating a broad class of 2D carbides and carbonitrides with single- and multivalent ions in electrochemical energy storage applications. Zhang, Kremer [141] used a simple, affordable, yet complex stamping technique to transform 2D $Ti_3C_2T_x$ MXene viscous ink into micro-supercapacitors (MSCs). A variety of stamp forms were 3D printed, covered in MXene ink, and then forcefully pressed onto paper substrates to test the efficacy of our approach. Furthermore, they demonstrate how to create intricately designed cylindrical/pad stamps that may be used to quickly build hundreds of MXene-based MSCs, illustrating a scaled-up manufacturing process. However, adopting this stamping technique to make all-MXene MSCs reduces both manufacturing cost and production time significantly when compared to inkjet printing or direct 3D printing, which often need specially prepared substrates and/or expensive equipment and procedures [142]. The fabricated solid-state $Ti_3C_2T_x$ MXene MSCs have a high areal capacitance (C/A) of 61 mF cm^{-2}, as well as a long lifespan, high energy density, and power density. The integration of printed-in 3D stamps and the MXene inks allows for the quick manufacturing of flexible all-MXene MSCs respectively. Importantly, they established two techniques to possibly increase manufacturing of these all-MXene MSCs using pad and cylindrical stamps. MSCs with a high areal capacitance (56.8 mF cm^{-2} at the scan rate of 10 mV/s) may be produced quickly by cold pressing or rolling. Whereas, higher areal and volumetric capacitance, as well as higher rate handling of the solid-state MSCs, can be achieved by further optimizing the MXene synthesis, surface chemistry, size of the MXene flakes and tuning the composition, or engineering the stamps' design, among different things, opening up exciting opportunities in the fabrication of printable energy storage devices correspondingly.

Lukatskaya, Kota [143] found that alternative electrode design tactics can bring MXene capacitance closer to its theoretical limit. Glassy carbon current collectors increased the operating potential window to 1 V in a 3 M H_2SO_4 electrolyte. The results obtained indicated that the expanded voltage window is not limited to glassy carbon but may also be accomplished using Ti foil or graphite current collectors. The fabricated macroporous electrode designs achieved exceptional capacitance retention at charge-discharge rates over 1 V s^{-1}: 210 F g^{-1} at 10 V s^{-1} and 100 F g^{-1} at the scan rate of 40 V s^{-1}, exceeding the highest quality carbon supercapacitors available respectively [144]. Hu, Li [145] used a simple dropping-mild baking (DMB) process to create self-assembled $Ti_3C_2T_x$ films from $Ti_3C_2T_x$ flakes suspension. The suspension was prepared by sonicating nanosheets derived from a porous Ti_3AlC_2 monolith. The resulting films developed for SCs exhibited impressive gravimetric capacitances, excellent cyclability, and rate performance.

5.1. MXene/polymer hybrid supercapacitors

Because of their long lifespan, ability to charge and discharge rapidly, and high power density (PD), electrochemical supercapacitors (ESCs) are among the most promising energy storage devices (ESDs) [146]. These devices can also be classified as EDLCs and pseudocapacitors based on the charge storage capabilities of the supercapacitors. Pseudocapacitors typically depend on a redox process at the electrode and electrolyte contact. Accordingly, they have a high energy density (ED) but a short cycle life. In contrast, charge transfer phenomena occur via ion desorption and adsorption in EDLCs, where the ions entirely disperse within the electrode–electrolyte surface [146]. Additionally, hybrid supercapacitors can maintain high ED among the PD and EDLCs and are equivalent to EDLCs by combining the qualities of a pseudocapacitor and an EDLC. There is much interest in creating cost-effective, high-performance electrode materials because of the low ED of supercapacitors. The derived material (2D, which gives rise to supercapacitor materials) has a variety of active sites, is atomically thin, and has useful mechanical properties. After the discovery of graphene, the highly demanding substance MXene performed well in supercapacitors, exhibiting high-capacity retention and rapid charge-discharge. Because of its high ED, volumetric capacitance, and elimination of the need for a metallic current collector, MXene electrodes have recently demonstrated high supercapacitor performance. A high volumetric capacitance of up to 350 F/cm^3 at 20 mV/s (and 450 F/cm^3 at 2 mV/s) in aqueous KOH was reported for a $Ti_3C_2T_x$ paper electrode, with essentially no deterioration after 10,000 cycles at 1 A/g (Fig. 12a,b) [140]. Similarly, as supercapacitor electrodes in an H_2SO_4 electrolyte, Ghidiu, Lukatskaya [115] used rolled films to evaluate the supercapacitor performance. After 10,000 cycles, there was no noticeable reduction in the electrochemical performance, and the device yielded a capacitance of up to 900 F/cm^3 or 245 F/g (Fig. 12c–e). This enhanced electrochemical performance resulted from several variables corresponding to surface redox processes, including the smaller size of H^+ relative to other intercalating b-cations and enhanced availability to the IL region because of the pre-intercalated water. Additionally, Xia, Mathis [122] discussed a 2D MXene-based electrode structure, analogous to the vertical arrangement as a supercapacitor electrode. When the MXene lamellar liquid crystal film thickness increased from 6 μm to 35 μm for filtered films, both the assembled parallel and vertical MXene films for pseudocapacitance continued to function in the same manner. Additionally, the same material exhibited an excellent cyclic life: close to 100 % capacity retention after ca. 20,000 charge–discharge cycles.

Moreover, the potential for MXene-based composites as SC electrodes is likewise substantial. Ling, Ren [148] recently reported the properties of a $Ti_3C_2T_x$/polymer composite film made by combining $Ti_3C_2T_x$ and PVA (Fig. 13a–f). The composite film demonstrated high volumetric capacitance when used as an electrode, reaching values of 528 F/cm^3 at 2 mV/s and 306 F/cm^3 at 100 mV/s in a KOH electrolyte. The volumetric capacitance of 314 F/cm^3 after 10,000 cycles remained considerable, suggesting the composite's sufficient cyclic stability despite a modest drop in capacitance over 10,000 cycles at 5 A/g.

MXene and carbon nanotube (CNT) dispersions were filtered to generate sandwich-like MXene/CNT composite paper electrodes. $Ti_3C_2T_x$/single-walled CNT paper attained a volumetric capacitance of ca. 345 F/cm^3 at 5 A/g, and after 10,000 cycles, no deterioration was observed for the material. In contrast, although $Ti_3C_2T_x$/multiwalled CNT paper generated a lower volumetric capacitance of 300 F/cm^3 at 10 A/g, this value increased to ca. 350 F/cm^3 after 10,000 cycles, possibly due to the increased accessibility of the slit pores. The electrolyte used to investigate these paper electrodes was $MgSO_4$, an ionic compound with relatively poor conductivity. As a result, adding appropriate electrolytes might further improve the electrode characteristics [117].

Similarly, Ling, Ren [148] investigated the performance of $Ti_3C_2T_x$/PVA composites. MXene increased the tensile strength of $Ti_3C_2T_x$/PVA composites. Impressive volumetric capacitance (528 F/cm^3 at 2 mV/s and 306 F/cm^3 at 100 mV/s) was also obtained upon using the composites as electrodes for supercapacitor in a KOH electrolyte. This capacitance was directly related to the MXene's increased IL spacing. Additionally, decentralized conjugated polymer (PDT)/MXene exhibited a high area capacitance of 284 mF/cm^3 at 50 mA/cm and low

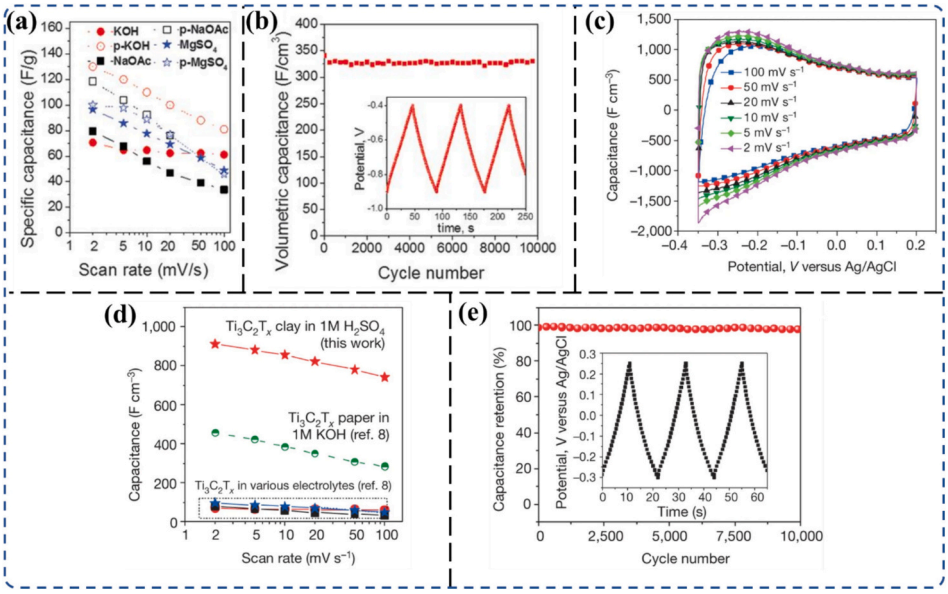

Fig. 12. a-b) Specific capacitance versus scan rate curve at various rates and retentivity evaluation of $Ti_3C_2T_x$ paper in an aqueous electrolyte: inset, GCD data storage at 1 A/g current density [140]. c–e) Electrochemical evaluation of rolled MXene films representing the CV profile at 2–100 mV/s scan rates, rate comparison performance of MXene by utilizing HF processing and cyclic performance test: inset, GCD curves at 10 A/g current density [115].

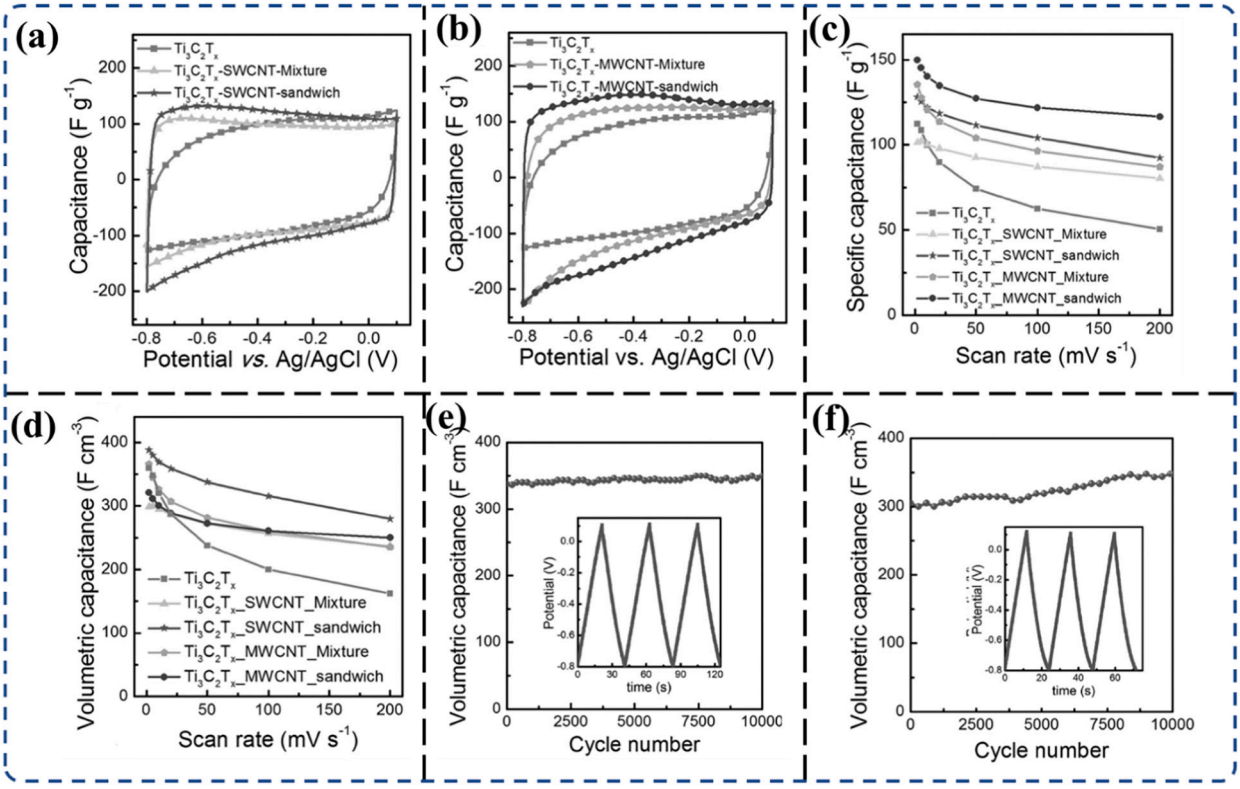

Fig. 13. a–f) CV plots of MXene and MXene/CNT composite electrodes; gravimetric capacitances and volumetric capacitances of $Ti_3C_2T_x$ and $Ti_3C_2T_x$/CNT electrodes at various scan rates. Cycling stability of sandwich-such as $Ti_3C_2T_x$/SWCNT and $Ti_3C_2T_x$/MWCNT electrodes at 10 A/g; the entire set of procedures was performed in aqueous 1 M $MgSO_4$ [148].

capacitance loss that even reached almost 100 % capacitance retention after 10,000 charge–discharge cycles [149]. Table 1 shows various MXene- and polymer-related materials used in high-performance supercapacitor applications.

In addition, Wu, Niu [152] reported organ-like MXene with PANI through chemical grafting for high-performance supercapacitors. Five electrodes were prepared in which N–Ti_3C_2–PANI-420 electrode attained a 228 F/g specific capacitance at a scan rate of 5 mV/s. Moreover, after 1000 charging/discharging cycles, the N–Ti_3C_2 material exhibited negligible attenuation, whereas PANI, N–Ti_3C_2, and N–Ti_3C_2/PANI-420 all exhibited between 82 % and 85 % capacitance retention. N–Ti_3C_2/PANI-420 exhibited higher cycling stability than PANI, which

Table 1
Overview of MXene/polymer-based materials for SC devices.

MXene/polymer-	Method	Electrolyte	Capacity retention	Specific capacity / specific or volumetric capacitance	Energy density (ED) / power density (PD)	Cycles	Ref.
MXene/PPy//MXene/PPy	Electrodeposition	1 M H_2SO_4	86.4 %	184 F/g at 10 mV/s	–	5000	[150]
MXene/PANI	Hydrothermal	6 M KOH	95.3 %	592 F/g at 0.5 A/g 477 F/g at 20 A/g	–	10,000	[151]
AC//MXene/PANI	Hydrothermal	7 M KOH	90.82 %	262 F/g, 0.5 A/g	22.67 Wh/kg at 217 W/kg	10,000	[151]
Ti_3C_2/PVA-KOH	Vacuum Assisted Filtration	1 M KOH	–	528 F/cm^3 at 2 mV/s	–	10,000	[148]
N-Ti_3C_2/PANI	Electrochemical Reaction Method	0.5 M H_2SO_4	85 %	228 mF/g at 5 mV/s	–	1000	[152]
TDP	Polymerization Method	1 M H_2SO_4	61 %	452 F/g at 1 A/g	–	2000	[153]
$Ti_3C_2T_x$/PPy	In-situ Polymerization	1 M Na_2SO_4	83.33 %	184 F/g at 2 mV/s	–	4000	[154]
PANI@MXene	Vacuum Assisted Filtration + Polymerization	3 M H_2SO_4	85.7 %	1632 F/cm^3 at 10 mV/s	–	20,000	[155]
MXene//PANI@MXene	Vacuum Assisted Filtration + Polymerization	3 M H_2SO_4	–	87 F/g, at 10 mV/s	50.6 Wh/L at 1.7 kW/L	–	[155]
PANI/MXene	Chemical oxidation polymerization	1 M H_2SO_4	87.5 %	1167 F cm^{-3} At 5 mV/s	PD = 1687.3 W/L ED = 65.6 Wh/L	5000	[156]
$Ti_3C_2T_x$/PANI-NTs	in situ polymerization	1 M H_2SO_4	94.7 %	597 F/g At 0.1 A/g	–	5000	[157]
Ti_3C_2/PANI-NTs//Ti_3C_2/PANI-NTs	in situ polymerization	1 M H_2SO_4	81.1 %	586 F/g, 0.1 A/g	PD = 153.2 W/kg ED = 25.6 Wh/kg	4000	[157]
3D-PMCF//3D-PMCF	Freeze-Drying	3 M H_2SO_4	95.9 %	375 F/g at 5 mV/s	9.2 Wh/kg	10,000	[158]
$Ti_3C_2T_x$//rGO/CNT/PANI	Etching + Polymerization	3 M H_2SO_4	80 %	117 F/g, 10 mV/s	70 Wh/L at 1.4 kW/L	10,000	[159]
$Mo_{1.33}C$ MXene/PEDOT: PSS	Vacuum Filtration	1 M H_2SO_4	–	1310 F/cm^3 at 2 mV/s	–	–	[160]
$Mo_{1.33}C$ MXene/PEDOT: PSS//$Mo_{1.33}C$ MXene/PEDOT: PSS	Vacuum Filtration	1 M H_2SO	90 %	568 F/g at 0.5 A/g	33.3 mWh/cm^3 at 19470 mW/cm^3	10,000	[160]
RAMX//RAMX	Vacuum Filtration and Evaporation	3 M H_2SO_4	91.14 %	736 F/cm^3 at 2000 mV/s	40 Wh/L at 0.83 kW/L	20,000	[161]
3D $Ti_3C_2T_x$@PPy	in situ polymerization	3 M KOH	100 %	610 F/g at 0.5 A/g	–	14,000	[162]
MXene/PANI (MP)	in situ polymerization	1 M H_2SO_4	91.2 %.	661 F/g	53.32 Wh/L(17.45 Wh/kg)	10,000	[163]
MXene/Ag NWs/cellulose	Vacuum filtration	PVA/H_2SO_4	90.9 %	505 F/g at 10 mV/s	–	500	[164]
PANI/$Ti_3C_2T_x$	Polymerization + Hummer's Method	1 mol·L^{-1} Na_2SO_4	80.4 %	462 F/g	50.8 Wh/kg (at 0.9 kW/kg)	5000	[165]
GMP	HF Etching + Polymerization	1 M H_2SO_4	97.54 %	635 F/g at 1 A/g	–	10,000	[166]
$Ti_3C_2T_x$/P-100-H//rGO	Etching + Polymerization + Hummer's Method	1 M H_2SO_4	–	117 F/cm^3, 1.5 mA/cm^2	23 mWh/cm^3 at 7659 mW/cm^3	–	[167]
$Ti_3C_2T_x$/CMC-PANI (TCP) film	in situ polymerization	1 M H_2SO_4	89.6 %	1161.4 mF/cm^2 at 1 mA/cm^2	158.7 μWh/cm^2 at 700.1 μW/cm^2	15,000	[168]
α-Fe_2O_3-C-MoS_2_PEDOT: PSS	Vacuum Filtration	1 M H_2SO_4	90.4 %	541 F/g	371 μWh/cm^2 at 1236 Wh/kg	10,000	[169]

might be attributable to the attractive chemical interactions between N–Ti_3C_2 and PANI as well as clearly defined organ-like nanostructures.

Zhang, Zhu [158] reported an in-situ ice template strategy for preparing 3D- porous MXene CNT films (PMCF)//3D–PMCF) symmetric device for supercapacitor performance. At scan rates ranging from 5 to 100 mV/s, cyclic voltammetry (CV) curves for the 3D–PMCF symmetric supercapacitors were captured (Fig. 14a–d). D–MF and 3D-PMF were also put together into symmetric supercapacitors for comparison. The 3D-PMCF symmetric supercapacitor confirms the outstanding endurance of high rate of capacitance and an excellent reversibility by exhibiting a pair of redox peaks without any discernible peak shape distortion as the scan rate increased, contrary to the D–MF symmetric SC. Additionally, the assembled symmetric supercapacitor specific capacitance varied with the scan rate from 5 to 10,000 mV/s. In comparison with its compositional counterparts, the 3D–PMCF symmetric supercapacitor exhibited the highest specific capacitance of 74.1 F/g at 5 mV/s. This is based on the combined mass of the anodic and cathodic electrodes. Additionally, the specific capacitance increased to 40.3 F/g, or ca. 3.4× that of the D–MF symmetric supercapacitor, as the scan rate increased to 1000 mV/s. The 3D–PMCF exhibited a symmetric supercapacitor cycle performance at 5 A/g of current density, respectively. The symmetric supercapacitor exhibited 86.3 % of its initial capacitance, indicative of long-term cycle stability. Ragone plots of 3D–PMCF, 3D–PMF, and D–MF symmetric supercapacitors indicate that 3D–PMCF reached its maximum energy density of 9.2 Wh/kg at a power density of 96.1 W/kg. Thus, a promising means of developing MXene-based flexible electrodes for supercapacitors is structural engineering from 2D $Ti_3C_2T_x$ to 3D architecture using the in-situ ice template approach. The measured competitive performance of 3D–PMCF indicates the superiority of its 3D porous network.

Besides symmetric and asymmetric devices, supercapattery was developed by combining two SC technologies: battery-graded electrodes and supercapacitors. This energy storage device provides tremendous power, high energy densities, and rapid charging and discharging capabilities. The increased cycle lifespan of supercapattery devices, which combine the benefits of supercapacitors with batteries, is a crucial feature [170–172]. It is evident that supercapatteries and battery-type technologies have different energy and power densities. Modern research is increasingly focused on enhancing the capacity of supercapacitor batteries for storing energy. Research is underway to develop new electrode materials that can store charge through electrochemical sensitivity and Faradic redox reactions. Because of the high specific

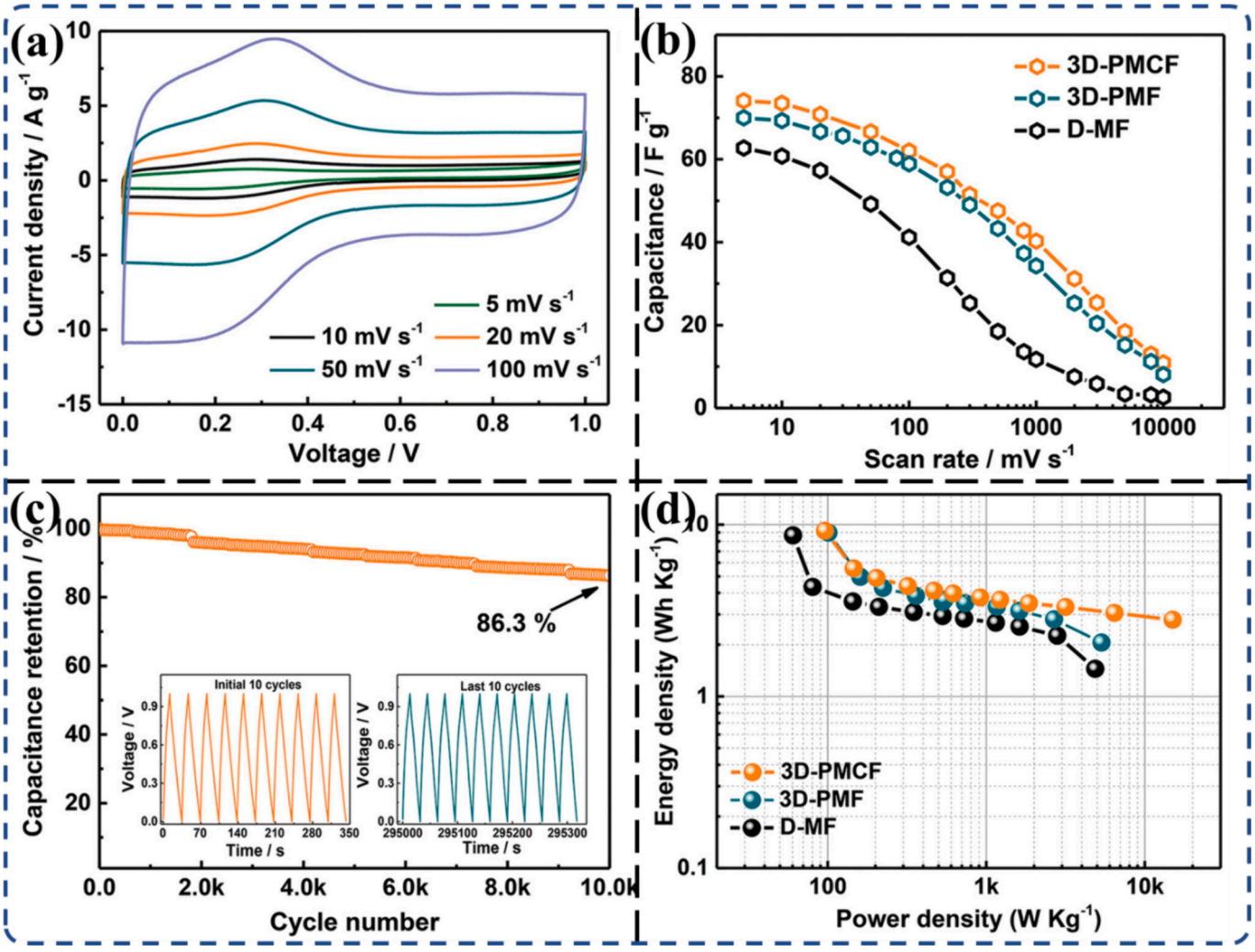

Fig. 14. Electrochemical characteristics of 3D PMCF-based symmetric supercapacitors: a) CV curves for 3D PMCF-based symmetric SCs, b) gravimetric capacitance of 3D PMCF and its competitive film electrodes, c) corresponding cycle performance measured for 10,000 cycles at s current density of 5 A/g, and d) Ragone plot profiles for 3D PMCF, 3D PMF, and 3D MF respectively [158].

power of the EDLC and the battery's long lifespan, there is the problem of using high potentials. Starting with the capacitive electrodes that modulate the redox behavior of the battery electrode, the supercapattery device improves not only the specific energy (Es) but also the specific power (Ps) [172–174].

MXene has also been widely used in supercapacity applications to produce high-performance ESDs. Nasrin, Subramani [175] synthesized manganese cobalt sulfide to produce titanium carbide (Ti_3C_4) MXene based on transition metal sulfides ($MnCo_2S_4$). Development in the field of transition metal sulfides with 2D MXene is an active field of research because of its highly conductive nature and high reversible redox activity. An evaluation of the supercapattery device electrochemical examination indicates an improved Qs of 600C/g at 1 A/g compared to pristine electrodes. The device exhibited high energy and power densities of 25.6 and 6400 W/kg after 12,000 GCD cycles, with stability retention of 100 %. For high-performance supercapattery applications, Iqbal, Ansari [176] described hydrothermal and in-situ oxidative aniline polymerization of PANI with CNTs and MnO_2. Electrochemical tests with as-prepared samples of PANI, CNT, and MnO_2 in comparison with pure MnO_2, PANI, and PANI@CNT indicate that the composite of PANI@CNT and MnO_2 performed better than either component alone. The PANI@CNT/MnO_2 ternary composite exhibited an excellent specific capacity of 143.26C/g at a scan rate of 3 mV/s. Additionally, the supercapattery (PANI@CNT/MnO_2/activated carbon)—comprised of a battery-type electrode—exhibited a cyclic stability of 119 % after the 3500 continuous charge and discharge cycles. Additionally, it exhibited a gradual increase in specific capacity after 1000 cycles of continuous charge–discharge (Fig. 15a–d).

6. MXene for batteries

Advanced battery materials such as anodes and cathodes can enhance the voltage window and ion storage capability to achieve an excellent ED of EVs, along with an extended driving pathway and durability. Therefore, bad conductive electrodes with an unstable solid electrolyte interphase (SEI) and more significant volume expansion are key in practical applications. Accordingly, the production of MXene over the past few decades has utilized conductive 2D substrates and active electrochemical materials for manufacturing novel functional electrodes. Therefore, intercalation and de-intercalation of alkali metal ions such as Na^+, Mg^{2+}, K^+, and Li^+ are essential considerations for the design and operation of rechargeable batteries [153,154]. The hydrophilic nature, electrical conductivity, and capability to use various cations render 2D MXene a promising electrode in rechargeable batteries [155]. Furthermore, controlling the interlayer (IL) spacing of MXene is feasible, thereby introducing surface functional group modifications. Several studies have explored the application of MXene and MXene-based composites in various contexts, including Li—S batteries (LSBs),

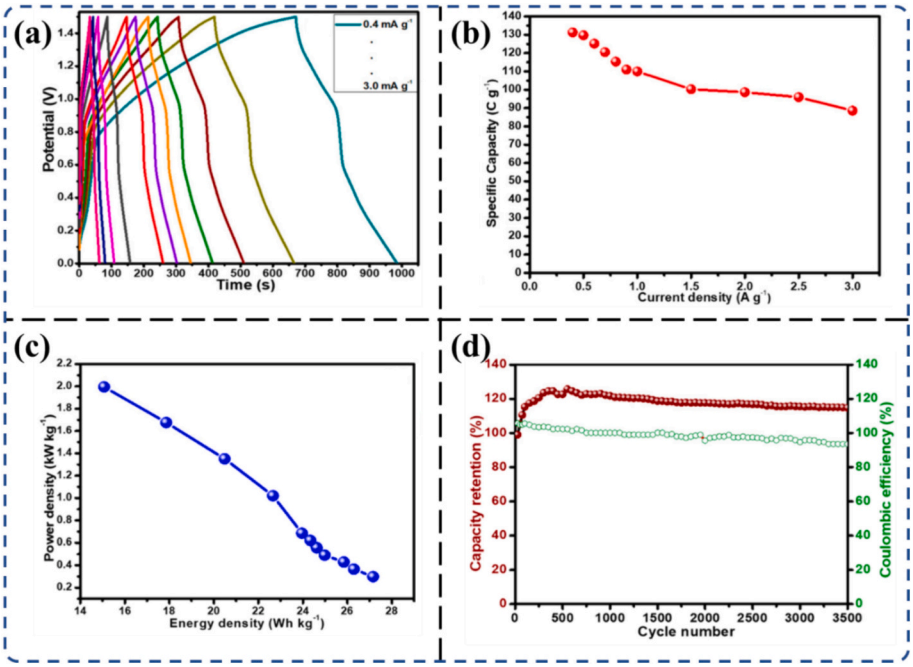

Fig. 15. a) GCD plot of PANI@CNT/MnO_2 ternary composite for the prepared hybrid device, b) current density versus specific capacity, c) Ragone plot, and d) cyclic performance and coulombic efficiency of the PANI@CNT/MnO_2 ternary composite-based hybrid device [176].

[156] Na-ion batteries (SIBs), [157] and LIBs [158,159].

LIBs are a promising candidate for upcoming energy conversion and storage devices based on their durability and specific energy. LIBs are crucial in portable electronic appliances and are common in electric vehicles [160]. Accordingly, substantial research has been reported on engineering the electrode material to optimize the charge storage capability with superior ionic and electronic conductivity for energetic LIBs.[161] Similarly, SIBs are especially important because of their low cost and lower redox potential than Na, rendering these batteries analogous to LIBs [162].

Yang, Ji [177] used DFT simulations to study the use of MXenes in sodium anode materials and concluded that their interaction with Na^+ is poor. MXenes have a reduced diffusion activation energy in SIB, indicating their potential as a high-power electrode material. However, the energy barrier of ion migration may be influenced by other variables. Zhao, Clites [178] have discovered that adding HCl and other common acids to the $Ti_3C_2T_x$ solution can lead the paper to wrinkle. As a result, they described a novel method to generate multidimensional porous MXene ($Ti_3C_2T_x$) by alkali-induced wrinkling of MXene nanoflakes. The chosen bases range from 0.5 to 24 mol LiOH, NaOH, KOH, and TBAOH. Experimental data indicate that NaOH has superior electrochemical performance compared to other bases. The SEM pictures of Na-c-$Ti_3C_2T_x$ reveal irregular macropores with a diameter of 100,400 nm. The pore wall is thin and made up of numerous sheets. However, this does not occur when more bases are added. Na-c-Ti_3CT_x has a specific capacity of 130 mAh g^{-1} after 500 cycles and can sustain 54 mAh g^{-1} after 1000 charge-discharge cycles at 1.5 A g^{-1}, indicating outstanding capacity retention. The Li-c-$Ti_3C_2T_x$ with LiOH exhibits the highest performance. After 300 cycles at 0.1 A g^{-1}, the capacity reaches around 160 mAh. This innovative approach to creating 3D porous MXene materials has applications in catalysis, biology, environment, etc. Zhao, Liu [179] created layered accordion-like Ti_3C_2 (L-Ti_3C_2) using the HF etching method, and they used it as a sulfur host. The accordion-like structure and low resistivity (0.05 Ω m) allowed the S/L-Ti_3C_2 composite to show good cycle performance and high capacity with a sulfur content of 57.6 %. In addition, Zhao, Zhu [180] detailed a novel approach utilizing a small, flexible sulfur/MXene electrode devoid of binders and conductive agents. In this configuration, 2D MXene, characterized by metallic conductivity, acts as both the conductive network and the structural backbone. Through a self-assembly process, the tiny sulfur molecules achieve intimate contact with the MXene material. Consequently, the resulting flexible electrode within the bendable Li—S cell exhibits remarkable flexibility and robust electrochemical performance. Tang, Zhou [181] expressed a theoretical specific capacity of 320 mAh g^{-1} for the Ti_3C_2 anode. However, terminating with F or OH reduced the theoretical capacity significantly to 130 or 67 mAh g^{-1}. Mashtalir, Naguib [182] found a capacity of 410 mAh g^{-1} for Ti_3C_2 "paper" anodes without binders at a 1C rate. Following intercalation with dimethyl sulfoxide and dispersion using a sonicator, the Ti_3C_2 colloidal solution was filtered to create the "paper."

6.1. *MXene/polymer hybrids for batteries*

MXene and polymer composites are developing as novel materials for battery applications, using the synergistic features of both components. MXenes bring high conductivity and mechanical strength, whilst polymers provide flexibility and structural stability. Incorporating MXene into polymer matrices can greatly improve battery electrochemical characteristics, including charge storage capacity and cycle stability [183,184]. These composites may be designed to provide lightweight, flexible electrodes that are perfect for improved energy storage devices and wearable electronics [185]. Furthermore, by keeping the MXene layers from restacking, the polymers in these composites preserve ion accessibility and improve overall electrochemical performance. However, establishing uniform dispersion of MXene inside the polymer and preserving electrical connection throughout the composite material is still crucial for maximizing performance and attaining long-term stability in battery applications [186]. Chen, Boota [187] reported MXene/poly(3,4-ethylenedioxythiophene) (PEDOT) hybrid composites prepared by self-initiated polymerization to enhance the Li-ion storage performance (Fig. 16a). The coulombic efficiency of the material was substantially enhanced; for the pristine MXene, the efficiency was 38 % and with PEDOT, it was 53 % (Fig. 16b). The same after 100 charge-discharge cycles exhibited an average capacity of 71 mAh/g for d-MXene/PEDOT at a rate of 1000 mA/g (Fig. 16c). In contrast, pristine-MXene exhibited a performance of 9 mAh/g at the same rate, ca. 14 %

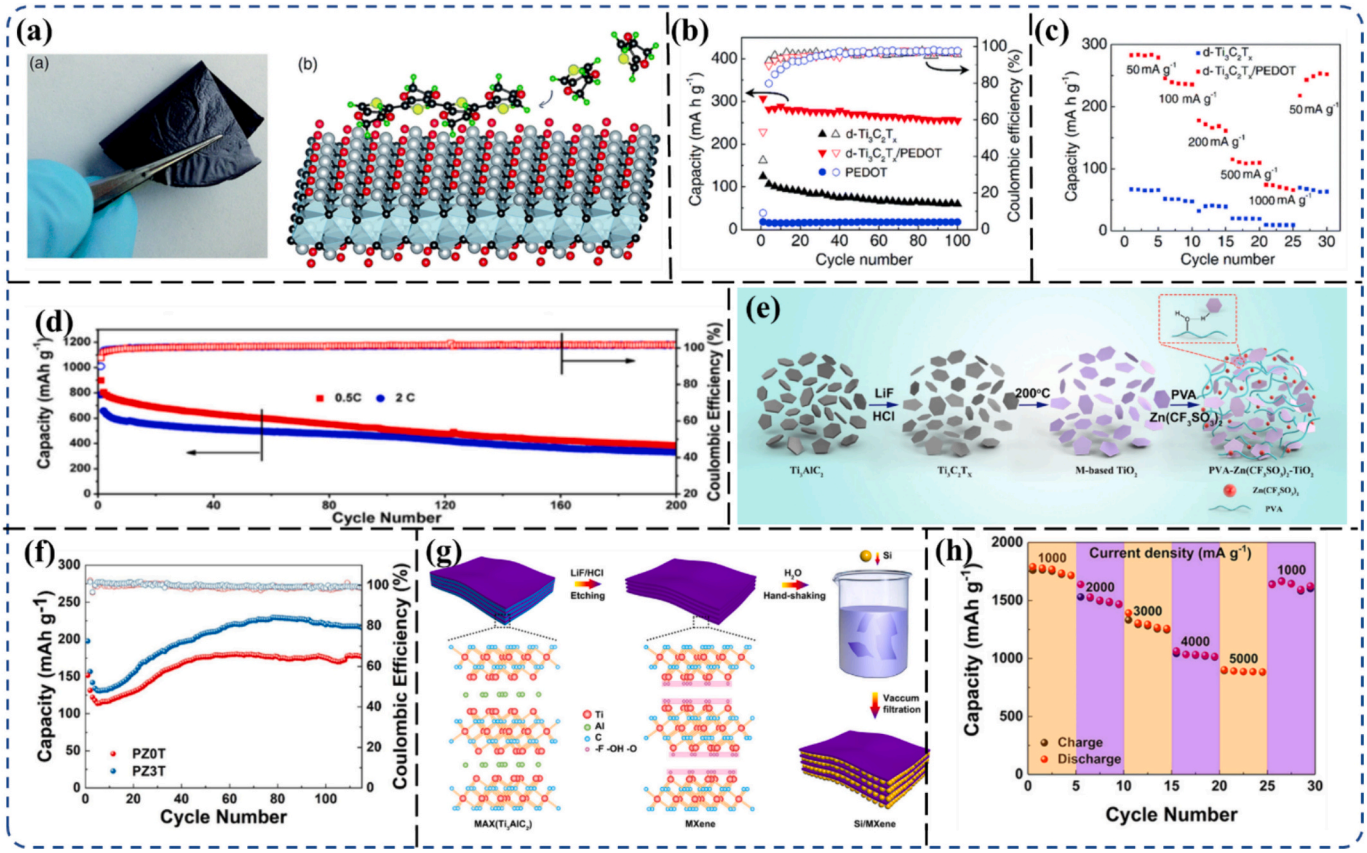

Fig. 16. a) Freestanding and flexible film of polymerized EDOT confined between MXene layers with a schematic of polymerized EDOT on the MXene surface [187]. b–c) Cyclic performance, and coulombic efficiency of the as-synthesized MXene–PEDOT in comparison with pristine MXene and rate performances of pure d-$Ti_3C_2T_x$ and d-$Ti_3C_2T_x$/PEDOT [187]. d) Long-term stability performance of the *a*-Ti_3C_2–S/d-Ti_3C_2/PP electrode tested at 0.5 and 2C [188]. e) Schematic for constructing a gel-polymer-based electrolyte with TiO_2 from $Ti_3C_2T_x$ MXene [189]. f) Coulombic efficiency and cyclic performance of the fabricated cell for Zn-ion batteries [189]. g-h) Schematic for fabricating Si/MXene composite paper and the rate ability performance of the material with respect to the total number of cycles [190].

of its capacity evaluated at 50 mA/g. The as-prepared materials also confirm that PEDOT in batteries initially served as the spacer that enhanced the excess of ions to the MXene layer concomitant with hybrid materials for proposed Li-ion capacitors. Similarly, Dong, Zheng [188] reported alkalized MXene with a polypropylene (PP) composite assembled by PP membrane filtration deposition and subsequently deposited S to fabricate Ti_3C_2 for Li—S batteries. Through this research, metal collectors were terminated to prevent further problematic integration. The fabricated material exhibited a reversible capacity of ca. 1062 mAh/g at a charge rate of 0.2C; improved compared with a battery

Table 2
Research on MXene/polymer-based materials for batteries focusing on rate performance.

MXene-polymer	Method	Capacity	Coulombic efficiency (%) or retention	Battery type	Ref
PVP-Sn(IV)@$Ti_3C_2T_x$	Vacuum Filtration	544 mAh/g at 0.5 A/g	–	Li-ion	[190]
PVHF/MXene-*g*-PMA	Chemical Grafting Technique	72.3 mAh/g at 2C	36.4 %	Solid zinc ion	[191]
MXene-bonded Si@C film	Vacuum filtration	2276.3 and 1660.6 mAh/g	73.0 %	Li-ion	[192]
$Ti_3C_2T_x$@PEI–CNTs/S	Phase Separation + Cross Linkage	1110 mAh/g at 0.5C	0.02 %@1500/1C	Li-S	[193]
$Ti_3C_2T_x$@PEI–CNTs interlayer	Phase Separation + Cross Linkage	1184 mAh/g/0.25C	0.286 %@100/0.25C	Li-S	[193]
HATN@MXene	Self-Standing and Binder-Free Method	233.6 mAh/g	93 %	Flexible proton battery	[194]
MXene@C/Polyolefin/MXene@C	Vacuum Filtration + Electrospinning	1159 mAh/g at 0.2C	95.8 %	Sodium-Sulfur Batteries	[195]
S@CMP	In situ polymerization	1402 mAh/g at 0.1C	98.7 %	Li–S	[196]
Li|PE-ZIF-8@MXene|$LiFePO_4$	In-situ Growth	–	89.6 %	Li-metal	[18]
PI@MXene	Solvent Replacement	115 mAh/g at 50 mA/g	–	Li-ion	[197]
MXene/Zn-(LDH)-array@PVA	Blade Coating	640.3 mAh/g	–	Zn–Air	[198]
(OMPDA)/$Ti_3C_2T_x$	In situ polymerization	430 mAh/g at 1000 mA/g	100 %	Li-ion	[199]
$Na_3V_2(PO_4)_3$/GPE/Na	Blending Method	93 mAh/g at 0.2C	95 %	Na battery	[200]
Si/Ti_3C_2	In situ orthosilicate hydrolysis	1849 mAh/g at 100 mA/g	87.8 %	Li-ion	[201]
Si/$Ti_3C_2T_x$ MXene	Electrostatic Self-Assembly	643.8 mAh/g at 300 mA/g	60.3 %	Li-ion	[202]
PDDA-NPCN/Ti_3C_2	Electrostatic Attraction Self-Assembly	358.4 mAh/g	95.9 %	PIB	[203]

with an MXene–S-based Al and electrode collector plate. Ti_3C_2–S/d-Ti_3C_2/PP yielded 47.7 % and 50.4 % cycling performance at 0.5 and 2C, respectively (Fig. 16d). Recently, Liu, Tian [189] reported an MXene-derived, 2D TiO_2-based hybrid gel electrolyte with polymer for solid-state Zn-ion batteries. The as-prepared material [full Zn||PVA–Zn $(CF_3SO_3)_2$–TiO_2||V_2O_5] in Fig. 16e exhibited 216 mAh/g of capacity. In addition, the material exhibited a coulombic efficiency of 99.8 % for the Zn||PZ_3T||V_2O_5 cell, which is higher than the efficiency of the Zn||PZ0T||V_2O_5 cell, i.e., 99.3 % (Fig. 16f). Tian, An [190] reported a free-standing MXene composite with silicone for high-performance LIBs. Binder-free silicone and MXene composite papers were harnessed via covalently anchoring Si NSs onto a conductive network based on MXene by vacuum filtration (Fig. 16g). The LIB material exhibited a rate performance of 890 mAh/g at 5000 mA/g cycles, confirming potential utility in high-performance batteries (Fig. 16h). Table 2 provides a detailed overview of MXene/polymer-based batteries and corresponding rate performance.

Hui, Zhao [201] reported an MXene composite with silicon (Si) for LIBs. They applied low-temperature reduction and in-situ orthosilicate hydrolysis for material preparation in which the tetraethyl hydrolysis orthosilicate yielded SiO_2 growth concomitant with homogenous nucleation on the MXene surface (Fig. 17a). Because of the MXene material, Si volume expansion and rapid charge transfer were observed among the electrons and Li^+. Additionally, the same material for LIB performance exhibited 1849 mAh/g of specific capacity at the rate of 100 mA/g. The same material maintained a capacity of ca. 956 mAh/g at a current density of 1 A/g (Fig. 17b). In another report by Zhang et al., [202], the same material was fabricated by electrostatic self-assembly for the potential LIBs (Fig. 17c). Similarly, Fig. 17d shows a specific capacity comparison of a Si–MXene anode with a pristine Si anode at 300 mA/g of current density. Pristine Si exhibited 2252.5 mAh/g of charge capacity in the first cycle, whereas the capacity suddenly decreased to 75.1 mAh/g after 100 charge cycles. The material also yielded an early reversible capacity of ca. 1067 mAh/g and reduced up to 638 mAh/g after the 100 charge–discharge cycles. In addition, the capacity retention was 60.3 % of the composite material, which is much higher than the bare Si and confirms the utility of the material for potential high-performance LIBs.

7. Challenges and future perspectives

MXene has become an increasingly active area of research because of its metal-like conductivity and substantial accessible ion surface area in a manner that resembles graphene. Following the identification of pseudocapacitive H^+ intercalation in $Ti_3C_2T_x$ MXene in 2014, MXene has been considered a promising electrode for energy storage devices, particularly in SCs and rechargeable batteries. However, supercapacitors with a comparatively large capacitance might be charged and discharged quickly using conducting polymers; which are also inexpensive, highly conductive, and environmentally acceptable electrodes. Thus, this article discusses current developments in SCs and batteries based on MXene/polymer nanocomposites, covering their synthetic pathways, characteristics, and applications. However, several challenges prevent widespread use of these materials in energy storage technology.

Firstly, MXene is safe and efficient, and dissolving multilayer MXene into individual flakes of MXene is cost-effective. However, the non-van der Waals IL interactions between the MAX phase layers necessitate harsh and dangerous chemical etching, which imparts difficulties in producing inexpensive and environmentally sustainable MXene/polymer nanocomposites on a large scale.

Second, incorporating MXene into the polymer matrix poses a challenge. Whereas MXene is an inorganic functional hydrophilic additive, most polymer products use hydrophobic polymers as their primary building blocks. The key challenge for further development will be to find a method of achieving exceptional blending performance of MXene in a hydrophobic polymer and MXene material, thus enabling innovative applications.

Preparing MXenes with a specific surface terminal group is a primary issue because MXene attributes strongly depend on the surface terminal groups; hence, functionalization of MXenes should be a future priority. Following DFT calculations, the surface terminal group can be changed to alter the band gap of MXenes [204]. Bare MXenes are metallic conductors, but those terminated with OH^- or F^- are open semiconductors with narrow band gaps [205]. Additionally, the terminal group has the ability to alter the $Ti_3C_2T_x$ MXene work function [206]. The work function can typically be increased by the —O group yet decreased by the –OH group. A thorough understanding of the work function remains

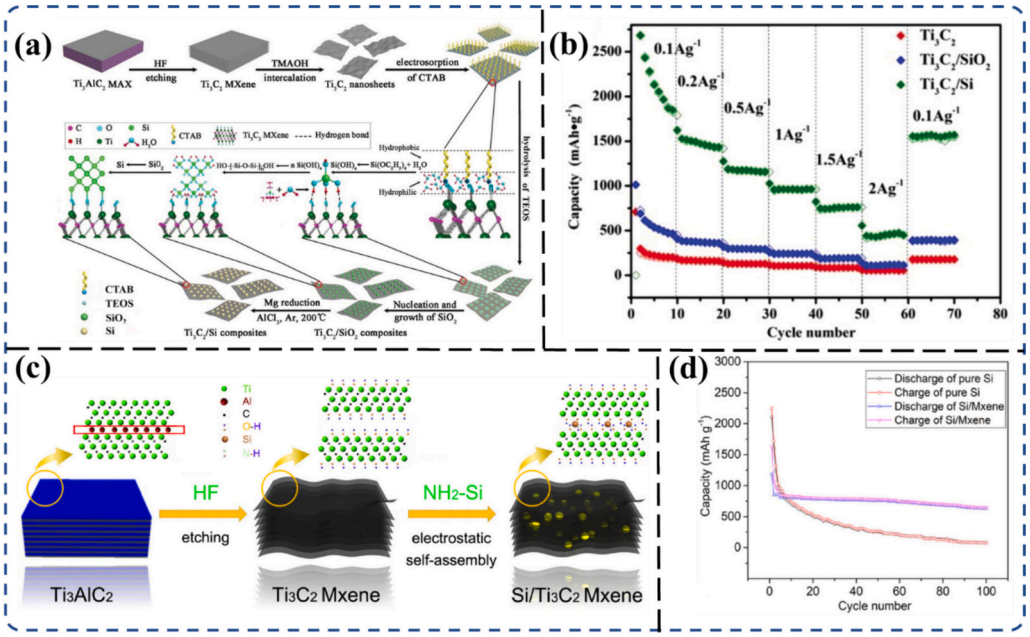

Fig. 17. a-b) Schematic for preparing a Ti_3C_2/Si composite; and rate performance profiles of Ti_3C_2, Ti_3C_2/SiO_2, and Ti_3C_2/Si electrodes [201]. c–d) Schematic of Si/$Ti_3C_2T_x$ MXene composite fabrication and cycling performance of a Si/$Ti_3C_2T_x$ MXene composite compared with bare Si [202].

elusive and will come from continued theoretical investigations.

Furthermore, MXene has a lower specific surface area than graphene for SCs, which might increase the energy density and specific capacitance of the material if increased by the same quantity. By using unique techniques—such as acid/base pathways—to induce pores into the electrodes, it is possible to exceed the limitations imparted by MXene's rigid nanosheets [207]. As a result, the energy density might be further increased by accommodating a wider variety of pseudocapacitive nanoparticles and fitting appropriate ions into high-voltage electrolytes. Incorporating MXene- and polymer-based flakes in the preparation poses a substantial challenge, resulting in a substantial reduction in surface utilization. To address this issue, implementing an IL spacer might be a feasible solution to prevent restacking of MXene flakes and consequently enhance their performance as electrode materials [208].

The most substantial difficulty is that most previous MXene research has been centered on polymer and MXene materials, as well as their composites with oxides, phosphates, sulfides, MOFs, and other substances. The utilization of MXene/polymer nanocomposites for ESD applications in supercapattery and supercapacitor technology presents promising benefits but is hindered by material limitations. Integrating battery-grade materials into these systems can potentially enhance energy and power density. The combination of MXene, known for its excellent hydrophilicity, with high-performance polymer-based materials could improve device performance, sparking interest in ESDs among emerging researchers. Despite inherent challenges, MXene/polymer nanocomposites have shown significant promise and utility in advancing this field.

Several strategies can be considered to address the challenges associated with the production and integration of MXenes into polymer composites. The hazardous chemical etching process currently used to exfoliate MXene layers is a key concern that requires attention. Exploring alternative, less hazardous exfoliation methods is crucial for improving the sustainability of MXene synthesis. Electrochemical etching under milder conditions could provide a viable alternative to the corrosive chemical approach. Additionally, physical techniques such as mechanical or ultrasonic exfoliation may offer a safer option despite being potentially less efficient. Novel methods utilizing biodegradable complexing agents or high-pressure annealing present promising avenues for safer MXene layer separation. Implementing chemical recycling in a closed-loop system could also help reduce waste and environmental impact. Long-term solutions may involve engineering safer MAX phase precursors that require gentler splitting conditions. Automating these safer production processes could enable scalable, efficient, and environmentally responsible MXene manufacturing.

Another critical challenge is improving the compatibility and dispersion of hydrophilic MXenes within hydrophobic polymer matrices. Surface functionalization of MXenes with hydrophobic groups can enhance their interactions with polymer chains, facilitating better integration. Incorporating compatibilizers or surfactants that can bridge the MXene-polymer interface may also improve the overall dispersion and stability of the nanocomposite. Employing advanced mixing techniques, such as ultrasonication or high-shear mixing, can further enhance the uniform distribution of MXenes within the polymer matrix. These strategies aim to maximize the interfacial bonding and homogeneous distribution of MXenes, ultimately improving the mechanical, electrical, and thermal properties of the resulting composite materials.

Precise control over the surface termination of MXenes is essential for tailoring their electrical properties, such as band gap and work function. Selective chemical modification techniques that attach specific functional groups (-OH, —F, —O) to the MXene surface can enable this tuning. Incorporating advanced deposition methods, such as atomic layer deposition (ALD) or chemical vapor deposition (CVD), may provide the necessary accuracy for such surface modifications. Computational techniques, like DFT simulations, can also aid in predicting the effects of different functional groups on the electrical characteristics of MXenes, allowing for systematic optimization of the materials for diverse applications, from electronics to energy storage.

As the field of MXene-polymer nanocomposites progresses, advancements in MXene exfoliation, dispersion, and surface engineering will be crucial. Ongoing research and simulations will help expand the understanding of MXene functionalization and its implications, further unlocking the potential of these materials for novel applications.

8. Conclusion

We provided a thorough overview and critical analysis of the most recent developments in the design of the various MXene and polymer harnessing techniques—and their diverse electrical, mechanical, and other properties—to address ongoing problems in energy storage. Several studies on 2D MXene have produced findings that demonstrate its flexibility, mechanical strength, thermal stability, chemical stability, hydrophilicity or hydrophobicity, superior electrical conductivity, and large surface area. Furthermore, composite materials comprised of MXene and polymers are frequently defined as bulk materials utilized as fillers or components, and both elements are distributed uniformly. In this article, we critically evaluated methods of manufacturing individual 2D MXenes (electrochemical, hydrothermal, and microwave synthesis) as well as MXene/polymer hybrid composites (in situ polymerization, hot or dry pressing, emulsion mixing, and solution blending) for energy storage. The surface chemistry, electrical, thermal, optical, magnetic, dielectric, and mechanical characteristics of MXene are substantially influenced by several factors, including the MAX phase purity, etchant, as well as etching and delamination. Thus, this article also describes the essential characteristics of MXene that relate to energy storage, with several potential research obstacles to facilitate the development of MXene/polymer hybrid composites. MXenes and MXene/polymer hybrid composites have demonstrated excellent properties for various energy storage applications. Nevertheless, many scientific challenges and unresolved issues must be addressed to fully exploit their exceptional capabilities in the most relevant SC and battery technologies. Critical indicators for practical battery use are cycling stability and energy density. Several strategies have been proposed to enhance these properties, including expanding the electrochemical window, increasing the output voltage, investigating novel electrode materials with high capacity and exceptional electronic conductivity, creating distinctive electrode architectures, as well as enhancing the aqueous electrolytes. These approaches hold promise for improving the cycling stability and energy density of MXenes as well as MXene/polymer hybrid composites, thereby advancing their utility in energy storage applications. It is critical to advance MXene preparation technologies; streamlining the preparation procedures and methodologies is essential for MXene/polymer hybrid composites to become widely used electrode materials for SCs and rechargeable batteries. Furthermore, there is a need for more research on MXenes with compositions and structures that are distinct from $Ti_3C_2T_x$; more studies on the oxidation of MXenes are required to address their susceptibility to oxidation, particularly during the preparation phase. Finally, it is essential to support their commercialisation to develop safer and environmentally sustainable processes for producing MXene/polymer hybrid composites, utilizing cost-effective precursors with improved efficiency. The combination of the MXene and polymer remains unoptimized; these composites hold immense potential as energy storage materials for automotive and grid applications. Therefore, concerted efforts must be undertaken to advance the field, facilitating the integration of MXene–polymer composites into next-generation energy storage systems.

Funding

The authors thank Sunway University's International Research Network Grant Scheme (STR-IRNGS-SET-GAMRG-01-2022).

CRediT authorship contribution statement

Hafiz Taimoor Ahmed Awan: Writing – original draft, Investigation, Formal analysis, Data curation. **Muhammad Amirul Aizat Mohd Abdah:** Writing – original draft, Visualization, Formal analysis, Data curation. **Maida Mehar:** Writing – review & editing, Visualization. **Rashmi Walvekar:** Writing – review & editing, Supervision. **Vishal Chaudhry:** Writing – review & editing, Methodology, Conceptualization. **Mohammad Khalid:** Writing – review & editing, Supervision, Resources, Methodology, Funding acquisition, Conceptualization. **Ajit Khosla:** Writing – review & editing, Supervision, Resources.

Declaration of competing interest

The authors declare that they have no known competing financial interests or personal relationships that could have appeared to influence the work reported in this paper.

Data availability

Data will be made available on request.

Acknowledgements

The authors acknowledge the support of Xidian University and Sunway University in carrying out this work.

References

[1] C. Han, W.-Q. Cao, M.-S. Cao, Hollow nanoparticle-assembled hierarchical $NiCo_2O_4$ nanofibers with enhanced electrochemical performance for lithium-ion batteries, Inorg. Chem. Front. 7 (21) (2020) 4101–4112.
[2] J. Wen, et al., Wearable technologies enable high-performance textile supercapacitors with flexible, breathable and wearable characteristics for future energy storage, Energy Stor. Mater. 37 (2021) 94–122.
[3] N. Wu, et al., Recent advances of asymmetric supercapacitors, Adv. Mater. Interfaces 8 (1) (2021) 2001710.
[4] L.E. Helseth, The self-discharging of supercapacitors interpreted in terms of a distribution of rate constants, J. Energy Storage 34 (2021) 102199.
[5] S. Ma, et al., Temperature effect and thermal impact in lithium-ion batteries: a review, Prog. Nat. Sci.: Mater. Int. 28 (6) (2018) 653–666.
[6] M. Mortada, et al., Impacts of reactant flow nonuniformity on fuel cell performance and scaling-up: comprehensive review, critical analysis and potential recommendations, Int. J. Hydrog. Energy 46 (63) (2021) 32161–32191.
[7] P. Kurzweil, Gaston Planté and his invention of the lead–acid battery—the genesis of the first practical rechargeable battery, J. Power Sources 195 (14) (2010) 4424–4434.
[8] I. Mohan, et al., Potential of potassium and sodium-ion batteries as the future of energy storage: recent progress in anodic materials, J. Energy Storage 55 (2022) 105625.
[9] M. Sarkar, A.R.M.H. Rashid, M. Hasanuzzaman, Beyond Li-ion batteries: future of sustainable large scale energy storage system, in: Reference Module in Materials Science and Materials Engineering, Elsevier, Amsterdam, Netherlands, 2022, pp. 595–604.
[10] W. Shao, et al., High-performance cobalt-doped carbon cloth supported porous Fe_2O_3 flexible electrode material in quasi-solid asymmetric supercapacitors, J. Alloys Compd. 929 (2022) 167141.
[11] Y. Yang, et al., High-performance hybrid supercapacitor enabled by advantageous heterojunction boosted starfish-like ZnCo-S electrode, J. Alloys Compd. 928 (2022) 166997.
[12] M. Shaker, et al., A criterion combined of bulk and surface lithium storage to predict the capacity of porous carbon lithium-ion battery anodes: lithium-ion battery anode capacity prediction, Carbon Lett. 31 (5) (2021) 985–990.
[13] Y. Chen, et al., MXene-based electrodes for supercapacitor energy storage, Energy Fuel 36 (5) (2022) 2390–2406.
[14] X. Wu, et al., Solvent-assisted self-assembly to fabricate a ternary flexible free-standing polyaniline@MXene-CNTs electrode for high-performance supercapacitors, J. Alloys Compd. 921 (2022) 166062.
[15] X. Li, et al., MXene-MnO_2-CoNi layered double hydroxides//activated carbon flexible asymmetric supercapacitor, J. Energy Storage 55 (2022) 105668.
[16] A. Wei, L. Wang, Z. Li, Metal-organic framework derived binary-metal oxide/MXene composite as sulfur host for high-performance lithium-sulfur batteries, J. Alloys Compd. 899 (2022) 163369.
[17] M.S. Javed, et al., Recent progress in the design of advanced MXene/metal oxides-hybrid materials for energy storage devices, Energy Stor. Mater. 53 (2022) 827–872.
[18] X. Zhao, et al., ZIF-8@MXene-reinforced flame-retardant and highly conductive polymer composite electrolyte for dendrite-free lithium metal batteries, J. Colloid Interface Sci. 620 (2022) 478–485.
[19] X. Wei, et al., The surface functional modification of $Ti_3C_2T_x$ MXene by phosphorus doping and its application in quasi-solid state flexible supercapacitor, Appl. Surf. Sci. 606 (2022) 154817.
[20] K. Liu, et al., Defect engineered $Ti_3C_2T_x$ MXene electrodes by phosphorus doping with enhanced kinetics for supercapacitors, Electrochim. Acta 435 (2022) 141372.
[21] H. Li, et al., 3D hierarchical transition-metal sulfides deposited on MXene as binder-free electrode for high-performance supercapacitors, J. Ind. Eng. Chem. 82 (2020) 309–316.
[22] M.S. Javed, et al., Heterostructured bimetallic–sulfide@layered Ti_3C_2T –MXene as a synergistic electrode to realize high-energy-density aqueous hybrid-supercapacitor, Nano Energy 101 (2022) 107624.
[23] W. Zhang, et al., Three-dimensional Ti_3C_2 MXene@silicon@nitrogen-doped carbon foam for high performance self-standing lithium-ion battery anodes, J. Electroanal. Chem. 921 (2022) 116664.
[24] S. Das, et al., A novel silicon-doped 2D Ti_2C MXene monolayer as high capacity stable anode material for lithium ion batteries: insight from density functional theory study, Appl. Surf. Sci. 600 (2022) 154173.
[25] M. Buffiere, D.S. Dhawale, F. El-Mellouhi, Chalcogenide materials and derivatives for photovoltaic applications, Energ. Technol. 7 (11) (2019) 1900819.
[26] S. Manzeli, et al., 2D transition metal dichalcogenides, Nat. Rev. Mater. 2 (8) (2017).
[27] R. Mas-Ballesté, et al., 2D materials: to graphene and beyond, Nanoscale 3 (1) (2011) 20–30.
[28] J.D. Caldwell, et al., Photonics with hexagonal boron nitride, Nat. Rev. Mater. 4 (8) (2019) 552–567.
[29] H. Lin, Y. Chen, J. Shi, Insights into 2D MXenes for versatile biomedical applications: current advances and challenges ahead, Adv. Sci. (Weinheim, Baden-Wurttemberg, Ger.) 5 (10) (2018), p. 1800518-1800518.
[30] C. Berger, et al., Electronic confinement and coherence in patterned epitaxial graphene, Science 312 (5777) (2006) 1191–1196.
[31] P.H. Cong, N.D. Duc, Postbuckling behavior of functionally graded multilayer graphene nanocomposite plate under mechanical and thermal loads on elastic foundations, VNU J. Sci.: Nat. Sci. Tech. 35 (4) (2019).
[32] H.S.S. Ramakrishna Matte, et al., MoS_2 and WS_2 analogues of graphene, Angew. Chem. Int. Ed. 49 (24) (2010) 4059–4062.
[33] P. Yan, et al., 2D amorphous-MoO_3−x@Ti_3C_2-MXene non-van der Waals heterostructures as anode materials for lithium-ion batteries, Nano Energy 86 (2021) 106139.
[34] M.W. Barsoum, The $M_{N+1}AX_N$ phases: a new class of solids, Prog. Solid State Chem. 28 (1–4) (2000) 201–281.
[35] Y. Gogotsi, B. Anasori, The rise of MXenes, ACS Nano 13 (8) (2019) 8491–8494.
[36] M. Naguib, et al., Two-dimensional nanocrystals produced by exfoliation of Ti_3AlC_2, Adv. Mater. 23 (37) (2011) 4248–4253.
[37] B. Anasori, M.R. Lukatskaya, Y. Gogotsi, 2D metal carbides and nitrides (MXenes) for energy storage, Nat. Rev. Mater. 2 (2) (2017) 1–17.
[38] Z.M. Sun, Progress in research and development on MAX phases: a family of layered ternary compounds, Int. Mater. Rev. 56 (3) (2011) 143–166.
[39] W. Sun, et al., Electrochemical etching of Ti_2AlC to Ti_2CT_x (MXene) in low-concentration hydrochloric acid solution, J. Mater. Chem. A 5 (41) (2017) 21663–21668.
[40] T. Yin, et al., Synthesis of $Ti_3C_2F_x$ MXene with controllable fluorination by electrochemical etching for lithium-ion batteries applications, Ceram. Int. 47 (20) (2021) 28642–28649.
[41] Z. Ma, et al., 3D porous MXene (Ti_3C_2)/reduced graphene oxide hybrid films for advanced lithium storage, ACS Appl. Mater. Interfaces 10 (4) (2018) 3634–3643.
[42] T. Guo, et al., Hydrothermal synthesis of MXene-MoS_2 composites for highly efficient removal of pesticides, Appl. Surf. Sci. 588 (2022) 152597.
[43] W. Luo, et al., H2O2 assisted hydrothermal oxidation of partially etched vanadium carbides (MXene) and their electrochemical properties as anode for Li-ion batteries, Appl. Surf. Sci. 523 (2020) 146387.
[44] S. Yang, et al., Fluoride-free synthesis of two-dimensional titanium carbide (MXene) using a binary aqueous system, Angew. Chem. 130 (47) (2018) 15717–15721.
[45] L. Xie, et al., Preparation and electrochemical performance of the layered cobalt oxide (Co_3O_4) as supercapacitor electrode material, J. Solid State Electrochem. 17 (1) (2013) 55–61.
[46] X. Chen, et al., MWCNT/V_2O_5 core/shell sponge for high areal capacity and power density Li-ion cathodes, ACS Nano 6 (9) (2012) 7948–7955.
[47] R.B. Rakhi, et al., Effect of Postetch annealing gas composition on the structural and electrochemical properties of Ti_2CT_x MXene electrodes for supercapacitor applications, Chem. Mater. 27 (15) (2015) 5314–5323.
[48] B. Ahmed, C. Xia, H.N. Alshareef, Electrode surface engineering by atomic layer deposition: a promising pathway toward better energy storage, Nano Today 11 (2) (2016) 250–271.
[49] A. Numan, et al., Microwave-assisted rapid MAX phase etching and delamination: a paradigm shift in MXene synthesis, Mater. Chem. Phys. 288 (2022) 126429.
[50] H. He, et al., Effect of electrolyte on supercapacitor performance of two-dimensional molybdenum carbide (Mo_2CT_x) MXene prepared by hydrothermal etching, Appl. Surf. Sci. 568 (2021) 150971.
[51] C. Wang, et al., HCl-based hydrothermal etching strategy toward fluoride-free MXenes, Adv. Mater. 33 (27) (2021) 2101015.

[52] K. Deshmukh, et al., Introduction to 2D MXenes: fundamental aspects, MAX phases and MXene derivatives, current challenges, and future prospects, Mxenes and their Composites (2022) 1–47.
[53] M. Naguib, et al., Two-dimensional transition metal carbides, ACS Nano 6 (2) (2012) 1322–1331.
[54] Y. Wu, et al., Few-layer MXenes delaminated via high-energy mechanical milling for enhanced sodium-ion batteries performance, ACS Appl. Mater. Interfaces 9 (45) (2017) 39610–39617.
[55] A. Lipatov, et al., Effect of synthesis on quality, electronic properties and environmental stability of individual monolayer Ti_3C_2 MXene flakes, Adv. Electron. Mater. 2 (12) (2016) 1600255.
[56] O. Mashtalir, et al., Intercalation and delamination of layered carbides and carbonitrides, Nat. Commun. 4 (1) (2013) 1–7.
[57] D. Zhao, et al., MXene (Ti_3C_2) vacancy-confined single-atom catalyst for efficient functionalization of CO_2, J. Am. Chem. Soc. 141 (9) (2019) 4086–4093.
[58] B. Salah, et al., Titanium carbide ($Ti_3C_2T_x$) MXene ornamented with palladium nanoparticles for electrochemical CO oxidation, Electroanalysis 34 (4) (2022) 677–683.
[59] A. Feng, et al., Two-dimensional MXene Ti_3C_2 produced by exfoliation of Ti_3AlC_2, Mater. Des. 114 (2017) 161–166.
[60] M. Ghidiu, et al., Synthesis and characterization of two-dimensional Nb_4C_3 (MXene), Chem. Commun. 50 (67) (2014) 9517–9520.
[61] M. Alhabeb, et al., Guidelines for synthesis and processing of two-dimensional titanium carbide ($Ti_3C_2T_x$ MXene), Chem. Mater. 29 (18) (2017) 7633–7644.
[62] P. Urbankowski, et al., Synthesis of two-dimensional titanium nitride Ti_4N_3 (MXene), Nanoscale 8 (22) (2016) 11385–11391.
[63] S.A. Melchior, et al., High-voltage symmetric supercapacitor based on 2D titanium carbide (MXene, Ti_2CT_x)/carbon Nanosphere composites in a neutral aqueous electrolyte, J. Electrochem. Soc. 165 (3) (2018) A501–A511.
[64] M.A. Hope, et al., NMR reveals the surface functionalisation of Ti_3C_2 MXene, Phys. Chem. Chem. Phys. 18 (7) (2016) 5099–5102.
[65] X. Zhan, et al., MXene and MXene-based composites: synthesis, properties and environment-related applications, Nanoscale Horiz. 5 (2) (2020) 235–258.
[66] K. Hantanasirisakul, Y. Gogotsi, Electronic and optical properties of 2D transition metal carbides and nitrides (MXenes), Adv. Mater. 30 (52) (2018) 1804779.
[67] Y.-Y. Peng, et al., All-MXene (2D titanium carbide) solid-state microsupercapacitors for on-chip energy storage, Energy Environ. Sci. 9 (9) (2016) 2847–2854.
[68] M. Malaki, A. Maleki, R.S. Varma, MXenes and ultrasonication, J. Mater. Chem. A 7 (18) (2019) 10843–10857.
[69] J. Zhu, et al., Rapid one-step scalable microwave synthesis of $Ti_3C_2T_x$ MXene, Chem. Commun. 57 (94) (2021) 12611–12614.
[70] S. Sun, et al., Rapid synthesis of polyimidazole functionalized MXene via microwave-irradiation assisted multi-component reaction and its iodine adsorption performance, J. Hazard. Mater. 420 (2021) 126580.
[72] Q. Zhao, et al., The design of Co_3S_4@MXene heterostructure as sulfur host to promote the electrochemical kinetics for reversible magnesium-sulfur batteries, Journal of Magnesium and Alloys 9 (1) (2021) 78–89.
[73] M. Ebrahimi, C.-T. Mei, Optoelectronic properties of $Ti_3C_2T_x$ MXene transparent conductive electrodes: microwave synthesis of parent MAX phase, Ceram. Int. 46 (18, Part A) (2020) 28114–28119.
[74] Y. Hu, et al., Biomass polymer-assisted fabrication of aerogels from MXenes with ultrahigh compression elasticity and pressure sensitivity, J. Mater. Chem. A 7 (17) (2019) 10273–10281.
[75] X.-P. Li, et al., Highly sensitive, reliable and flexible piezoresistive pressure sensors featuring polyurethane sponge coated with MXene sheets, J. Colloid Interface Sci. 542 (2019) 54–62.
[76] C. Lan, et al., Ultrathin MXene/polymer coatings with an alternating structure on fabrics for enhanced electromagnetic interference shielding and fire-resistant protective performances, ACS Appl. Mater. Interfaces 13 (32) (2021) 38761–38772.
[77] A. Levitt, et al., MXene-based fibers, yarns, and fabrics for wearable energy storage devices, Adv. Funct. Mater. 30 (47) (2020) 2000739.
[78] H. Yang, et al., Layered PVB/$Ba_3Co_2Fe_{24}O_{41}$/Ti_3C_2 Mxene composite: enhanced electromagnetic wave absorption properties with high impedance match in a wide frequency range, Mater. Chem. Phys. 200 (2017) 179–186.
[79] Y. Guo, et al., A wearable transient pressure sensor made with MXene nanosheets for sensitive broad-range human–machine interfacing, Nano Lett. 19 (2) (2019) 1143–1150.
[80] C. Zhang, et al., Two-dimensional transition metal carbides and nitrides (MXenes): synthesis, properties, and electrochemical energy storage applications, Energy Environ. Mater. 3 (1) (2020) 29–55.
[81] Z.A.A. Ghaleb, M. Jaafar, A.A. Rashid, Fabrication methods of carbon-based rubber nanocomposites and their applications, Carbon-Based Nanofillers Their Rubber Nanocompos. (2019) 49–63.
[82] Y. Liu, et al., $Ti_3C_2T_x$ filler effect on the proton conduction property of polymer electrolyte membrane, ACS Appl. Mater. Interfaces 8 (31) (2016) 20352–20363.
[83] M. Boota, et al., Interaction of polar and nonpolar polyfluorenes with layers of two-dimensional titanium carbide (MXene): intercalation and pseudocapacitance, Chem. Mater. 29 (7) (2017) 2731–2738.
[84] M. Naguib, et al., $Ti_3C_2T_x$ (MXene)–polyacrylamide nanocomposite films, RSC Adv. 6 (76) (2016) 72069–72073.
[85] J.-Y. Si, et al., Functionalization of MXene nanosheets for polystyrene towards high thermal stability and flame retardant properties, Polymers 11 (6) (2019) 976.
[86] B. Yu, et al., Interface decoration of exfoliated MXene ultra-thin nanosheets for fire and smoke suppressions of thermoplastic polyurethane elastomer, J. Hazard. Mater. 374 (2019) 110–119.
[87] X.H. Wang, Y.C. Zhou, Stability and selective oxidation of aluminum in nano-laminate Ti_3AlC_2 upon heating in argon, Chem. Mater. 15 (19) (2003) 3716–3720.
[88] Q. Pan, et al., 2D MXene-containing polymer electrolytes for all-solid-state lithium metal batteries, Nanoscale Adv. 1 (1) (2018) 395–402.
[89] Y. Tong, et al., Hybridizing polypyrrole chains with laminated and two-dimensional $Ti_3C_2T_x$ toward high-performance electromagnetic wave absorption, Appl. Surf. Sci. 434 (2018) 283–293.
[90] Z. Chen, et al., Preparation and electrochemical performances of doped MXene/poly(3,4-ethylenedioxythiophene) composites, Mater. Lett. 220 (2018) 305–308.
[91] H. Wei, et al., $Ti_3C_2T_x$ MXene/polyaniline (PANI) sandwich intercalation structure composites constructed for microwave absorption, Compos. Sci. Technol. 169 (2019) 52–59.
[92] L. Qin, et al., Polymer-MXene composite films formed by MXene-facilitated electrochemical polymerization for flexible solid-state microsupercapacitors, Nano Energy 60 (2019) 734–742.
[93] M. Carey, et al., Nylon-6/$Ti_3C_2T_z$ MXene nanocomposites synthesized by in situ ring opening polymerization of ε-caprolactam and their water transport properties, ACS Appl. Mater. Interfaces 11 (22) (2019) 20425–20436.
[94] L. Wang, et al., Fabrication on the annealed $Ti_3C_2T_x$ MXene/epoxy nanocomposites for electromagnetic interference shielding application, Compos. Part B 171 (2019) 111–118.
[95] R. Liu, et al., Ultrathin biomimetic polymeric $Ti_3C_2T_x$ MXene composite films for electromagnetic interference shielding, ACS Appl. Mater. Interfaces 10 (51) (2018) 44787–44795.
[96] H. Wang, et al., In situ polymerized $Ti_3C_2T_x$/PDA electrode with superior areal capacitance for supercapacitors, J. Alloys Compd. 778 (2019) 858–865.
[97] M. Boota, et al., Pseudocapacitive electrodes produced by oxidant-free polymerization of pyrrole between the layers of 2D titanium carbide (MXene), Adv. Mater. 28 (7) (2016) 1517–1522.
[98] L. Gao, et al., Optical properties of few-layer Ti_3CN MXene: from experimental observations to theoretical calculations, ACS Nano 16 (2) (2022) 3059–3069.
[99] A.E. Ghazaly, et al., Ultrafast, one-step, salt-solution-based acoustic synthesis of Ti(3)C(2) MXene, ACS Nano 15 (3) (2021) 4287–4293.
[100] Q. Zhao, et al., Flexible 3D porous MXene foam for high-performance lithium-ion batteries, Small 15 (51) (2019) 1904293.
[101] M. Hu, et al., Surface functional groups and interlayer water determine the electrochemical capacitance of $Ti_3C_2T_x$ MXene, ACS Nano 12 (4) (2018) 3578–3586.
[102] J. Zhou, et al., Synthesis and electrochemical properties of two-dimensional hafnium carbide, ACS Nano 11 (4) (2017) 3841–3850.
[103] S. Dong, et al., Dielectric-electrolyte supercapacitors, Cell Reports Physical Science 4 (2) (2023) 101284.
[104] S. Sharma, P. Chand, Supercapacitor and electrochemical techniques: a brief review, Results in Chemistry 5 (2023) 100885.
[105] N. Shirshova, et al., Structural composite supercapacitors, Compos. A: Appl. Sci. Manuf. 46 (2013) 96–107.
[106] S. Zhang, et al., Electrochemomechanical degradation of high-capacity battery electrode materials, Prog. Mater. Sci. 89 (2017) 479–521.
[107] X. Wang, et al., Structure and electromagnetic properties of $Ti_3C_2T_x$ MXene derived from Ti_3AlC_2 with different microstructures, Ceram. Int. 47 (10) (2021) 13628–13634.
[108] G. Xu, et al., Solvent-regulated preparation of well-intercalated $Ti_3C_2T_x$ MXene nanosheets and application for highly effective electromagnetic wave absorption, Nanotechnology 29 (35) (2018) 355201.
[109] G. Cui, et al., Synthesis and microwave absorption of $Ti_3C_2T_x$ MXene with diverse reactant concentration, reaction time, and reaction temperature, Ceram. Int. 45 (17) (2019) 23600–23610.
[110] M. Gounzari, et al., Mechanical characterization of nanoporous two-dimensional Ti3C2 MXene membranes, Chin. J. Phys. 80 (2022) 275–284.
[111] Halper, M.S. and J.C. Ellenbogen. Supercapacitors: A Brief Overview.
[112] P. Gupta, et al., Layer-resolved mechanical degradation of a Ni-rich positive electrode, Batteries 9 (2023), https://doi.org/10.3390/batteries9120575.
[113] S.E. Root, et al., Mechanical properties of organic semiconductors for stretchable, highly flexible, and mechanically robust electronics, Chem. Rev. 117 (9) (2017) 6467–6499.
[114] S. Panda, et al., MXene based emerging materials for supercapacitor applications: recent advances, challenges, and future perspectives, Coord. Chem. Rev. 462 (2022) 214518.
[115] M. Ghidiu, et al., Conductive two-dimensional titanium carbide 'clay' with high volumetric capacitance, Nature 516 (7529) (2014) 78–81.
[116] Y. Bai, et al., Dependence of elastic and optical properties on surface terminated groups in two-dimensional MXene monolayers: a first-principles study, RSC Adv. 6 (42) (2016) 35731–35739.
[117] M.-Q. Zhao, et al., Flexible MXene/carbon nanotube composite paper with high volumetric capacitance, Adv. Mater. 27 (2) (2015) 339–345.
[118] D. He, et al., Tribological properties of $Ti_3C_2T_x$ MXene reinforced interpenetrating polymers network coating, Tribol. Int. 163 (2021) 107196.
[119] A. Jabbar, et al., Nanocellulose coated woven jute/green epoxy composites: characterization of mechanical and dynamic mechanical behavior, Compos. Struct. 161 (2017) 340–349.
[120] W.-T. Cao, et al., Binary strengthening and toughening of MXene/cellulose nanofiber composite paper with nacre-inspired structure and superior

electromagnetic interference shielding properties, ACS Nano 12 (5) (2018) 4583–4593.
[121] D. Zhou, et al., 3D interconnected networks of a ternary hierarchical carbon nanofiber/MnO_2/$Ni(OH)_2$ architecture as integrated electrodes for all-solid-state supercapacitors, RSC Adv. 6 (76) (2016) 71882–71892.
[122] Y. Xia, et al., Thickness-independent capacitance of vertically aligned liquid-crystalline MXenes, Nature 557 (7705) (2018) 409–412.
[123] A. Berrueta, et al., Supercapacitors: electrical characteristics, modeling, applications, and future trends, IEEE Access 7 (2019) 50869–50896.
[124] X. Zhao, et al., The role of nanomaterials in redox-based supercapacitors for next generation energy storage devices, Nanoscale 3 (3) (2011) 839–855.
[125] B. Arumugam, et al., An Overview of active electrode materials for the efficient high-performance supercapacitor application, Crystals 13 (2023), https://doi.org/10.3390/cryst13071118.
[126] A.P. Khedulkar, et al., Sustainable high-energy supercapacitors: metal oxide-agricultural waste biochar composites paving the way for a greener future, Journal of Energy Storage 77 (2024) 109723.
[127] D. Tie, et al., Hybrid energy storage devices: advanced electrode materials and matching principles, Energy Storage Materials 21 (2019) 22–40.
[128] G.R. Berdiyorov, Effect of surface functionalization on the electronic transport properties of Ti_3C_2 MXene, Europhys. Lett. 111 (6) (2015) 67002.
[129] Y. Xie, P.R.C. Kent, Hybrid density functional study of structural and electronic properties of functionalized $Ti_{n+1}X_n$ (X = C, N) monolayers, Phys. Rev. B 87 (23) (2013).
[130] U. Ghanekar Sunita, S. Meena, Heteroatom induced tailoring electronic and optical properties of V_3C_2 MXene through bandgap opening: a computational insight, Chem. Phys. Lett. 799 (2022) 139639.
[131] A. Mostafaei, M. Abbasnejad, Computational studies on the structural, electronic and optical properties of M_2CT_2 (M=Y, Sc and T=F, Cl) MXene monolayer, J. Alloys Compd. 857 (2021) 157982.
[132] W. Zhang, et al., Atomic-scale investigation of electronic properties and Na storage performance of $Ti_3C_2T_x$-MXene bilayers with various terminations, Appl. Surf. Sci. 567 (2021) 150735.
[133] E.A. Mayerberger, et al., Preparation and characterization of polymer-$Ti_3C_2T_x$ (MXene) composite nanofibers produced via electrospinning, J. Appl. Polym. Sci. 134 (37) (2017) 45295.
[134] M. Fei, et al., Polybenzimidazole/Mxene composite membranes for intermediate temperature polymer electrolyte membrane fuel cells, Nanotechnology 29 (3) (2017) 035403.
[135] X.-H. Cui, et al., Theoretical insight into the electronic, optical, and photocatalytic properties and quantum capacitance of Sc_2CT_2 (T = F, P, Cl, Se, Br, O, Si, S, OH) MXenes, Vacuum 207 (2022) 111615.
[136] H. Chibani, et al., Revealing structural, mechanical, and electronic properties of M_4C_3 (M = Sc, Ti, Zr, Mo, Hf, and W) MXene monolayers based on first-principle calculations, Comput. Condens. Matter 32 (2022) e00713.
[137] J.H. Ciou, S. Li, P.S. Lee, Ti_3C_2 MXene paper for the effective adsorption and controllable release of aroma molecules, Small 15 (38) (2019) 1903281.
[138] C.J. Zhang, et al., Transparent, flexible, and conductive 2D titanium carbide (MXene) films with high volumetric capacitance, Adv. Mater. 29 (36) (2017) 1702678.
[139] L. Qian, et al., The flame retardant group-synergistic-effect of a phosphaphenanthrene and triazine double-group compound in epoxy resin, J. Appl. Polym. Sci. 131 (3) (2014) p. n/a-n/a.
[140] M.R. Lukatskaya, et al., Cation intercalation and high volumetric capacitance of two-dimensional titanium carbide, Science 341 (6153) (2013) 1502–1505.
[141] C. Zhang, et al., Stamping of flexible, coplanar micro-supercapacitors using MXene inks, Adv. Funct. Mater. 28 (9) (2018) 1705506.
[142] Q. Zhang, et al., Gravure-printed interdigital microsupercapacitors on a flexible polyimide substrate using crumpled graphene ink, Nanotechnology 27 (10) (2016) 105401.
[143] M.R. Lukatskaya, et al., Ultra-high-rate pseudocapacitive energy storage in two-dimensional transition metal carbides, Nat. Energy 2 (8) (2017) 17105.
[144] D. Pech, et al., Ultrahigh-power micrometre-sized supercapacitors based on onion-like carbon, Nat. Nanotechnol. 5 (9) (2010) 651–654.
[145] M. Hu, et al., Self-assembled $Ti_3C_2T_x$ MXene film with high gravimetric capacitance, Chem. Commun. 51 (70) (2015) 13531–13533.
[146] P. Simon, Y. Gogotsi, Perspectives for electrochemical capacitors and related devices, Nat. Mater. 19 (11) (2020) 1151–1163.
[148] Z. Ling, et al., Flexible and conductive MXene films and nanocomposites with high capacitance, Proc. Natl. Acad. Sci. USA 111 (47) (2014) 16676–16681.
[149] X. Wu, et al., Highly flexible and low capacitance loss supercapacitor electrode based on hybridizing decentralized conjugated polymer chains with MXene, Chem. Eng. J. 378 (2019) 122246.
[150] X. Jian, et al., Three-dimensional carambola-like MXene/polypyrrole composite produced by one-step co-electrodeposition method for electrochemical energy storage, Electrochim. Acta 318 (2019) 820–827.
[151] Y. Li, P. Kamdem, X.-J. Jin, Hierarchical architecture of MXene/PANI hybrid electrode for advanced asymmetric supercapacitors, J. Alloys Compd. 850 (2021) 156608.
[152] W. Wu, et al., Organ-like Ti_3C_2 Mxenes/polyaniline composites by chemical grafting as high-performance supercapacitors, J. Electroanal. Chem. 847 (2019) 113203.
[153] Z. Chen, et al., Preparation of polyaniline onto dl-tartaric acid assembled MXene surface as an electrode material for supercapacitors, ACS Appl. Energy Mater. 3 (9) (2020) 9326–9336.
[154] W. Wu, et al., Enhanced electrochemical performances of organ-like Ti3C2 MXenes/polypyrrole composites as supercapacitors electrode materials, Ceram. Int. 45 (6) (2019) 7328–7337.
[155] K. Li, et al., An ultrafast conducting polymer@MXene positive electrode with high volumetric capacitance for advanced asymmetric supercapacitors, Small 16 (4) (2020) 1906851.
[156] Y. Wang, et al., Scalable fabrication of polyaniline nanodots decorated MXene film electrodes enabled by viscous functional inks for high-energy-density asymmetric supercapacitors, Chem. Eng. J. 405 (2021) 126664.
[157] W. Wu, et al., Facile strategy of hollow polyaniline nanotubes supported on Ti_3C_2-MXene nanosheets for high-performance symmetric supercapacitors, J. Colloid Interface Sci. 580 (2020) 601–613.
[158] P. Zhang, et al., In situ ice template approach to fabricate 3D flexible MXene film-based electrode for high performance Supercapacitors, Adv. Funct. Mater. 30 (47) (2020) 2000922.
[159] K. Li, et al., All-pseudocapacitive asymmetric MXene-carbon-conducting polymer supercapacitors, Nano Energy 75 (2020) 104971.
[160] L. Qin, et al., High-performance ultrathin flexible solid-state Supercapacitors based on solution processable $Mo_{1.33}C$ MXene and PEDOT:PSS, Adv. Funct. Mater. 28 (2) (2018) 1703808.
[161] Z. Wu, et al., Reassembly of MXene hydrogels into flexible films towards compact and ultrafast Supercapacitors, Adv. Funct. Mater. 31 (41) (2021) 2102874.
[162] T.A. Le, N.Q. Tran, Y. Hong, H. Lee, Intertwined titanium carbide MXene within a 3 D tangled Polypyrrole nanowires matrix for enhanced supercapacitor performances, Chem. Eur. J. 25 (2019) 1037–1043.
[163] C. Li, et al., Sandwich-like high-load MXene/polyaniline film electrodes with ultrahigh volumetric capacitance for flexible supercapacitors, J. Colloid Interface Sci. 620 (2022) 35–46.
[164] H. Tang, et al., Scalable manufacturing of leaf-like MXene/Ag NWs/cellulose composite paper electrode for all-solid-state supercapacitor, EcoMat 4 (6) (2022).
[165] J. Zhou, et al., Ultrahigh rate capability of 1D/2D polyaniline/titanium carbide (MXene) nanohybrid for advanced asymmetric supercapacitors, Nano Res. 15 (1) (2022) 285–295.
[166] J. Fu, et al., Architecturally robust graphene-encapsulated MXene Ti_2CT_x@polyaniline composite for high-performance pouch-type asymmetric supercapacitor, ACS Appl. Mater. Interfaces 10 (40) (2018) 34212–34221.
[167] L. Li, et al., Flexible $Ti_3C_2T_x$/PEDOT:PSS films with outstanding volumetric capacitance for asymmetric supercapacitors, Dalton Trans. 48 (5) (2019) 1747–1756.
[168] H. Xu, et al., MXene/carboxymethylcellulose-polyaniline ($Ti_3C_2T_x$/CMC-PANI) film as flexible electrode for high-performance asymmetric supercapacitors, Electrochim. Acta 436 (2022) 141408.
[169] C. Li, et al., Sandwich-like MXene/α-Fe_2O_3–C–MoS_2-PEDOT:PSS/MXene film electrodes with ultrahigh area capacitance for flexible Supercapacitors, ACS Appl. Mater. Interfaces 14 (7) (2022) 9172–9182.
[170] B.K. Kim, et al., Electrochemical Supercapacitors for energy storage and conversion, in: Handbook of Clean Energy Systems, John Wiley & Sons, Ltd, 2015, pp. 1–25.
[171] C.-Z. Zhao, et al., Liquid phase therapy to solid electrolyte–electrode interface in solid-state Li metal batteries: a review, Energy Stor. Mater. 24 (2020) 75–84.
[172] B.E. Conway, Electrochemical Supercapacitors: Scientific Fundamentals and Technological Applications, Springer Science & Business Media, Germany, 2013.
[173] M.S. Halper, J.C. Ellenbogen, Supercapacitors: A Brief Overview, The MITRE Corporation, McLean, Virginia, VA, USA, 2006.
[174] M. Gusain, I. Ahmed, Y. Zhan, Conducting polymeric nanocomposite for supercapattery, Adv. Supercapacitor Supercapattery (2021) 63–91.
[175] K. Nasrin, et al., $MnCo_2S_4$ – MXene: a novel hybrid electrode material for high performance long-life asymmetric supercapattery, J. Colloid Interface Sci. 600 (2021) 264–277.
[176] J. Iqbal, et al., Hydrothermally assisted synthesis of porous polyaniline@carbon nanotubes-manganese dioxide ternary composite for potential application in supercapattery, Polymers 12 (12) (2020) 2918.
[177] E. Yang, et al., Exploring the possibilities of two-dimensional transition metal carbides as anode materials for sodium batteries, Phys. Chem. Chem. Phys. 17 (7) (2015) 5000–5005.
[178] D. Zhao, et al., Alkali-induced crumpling of $Ti_3C_2T_x$ (MXene) to form 3D porous networks for sodium ion storage, Chem. Commun. 54 (36) (2018) 4533–4536.
[179] X. Zhao, et al., Fabrication of layered Ti_3C_2 with an accordion-like structure as a potential cathode material for high performance lithium–sulfur batteries, J. Mater. Chem. A 3 (15) (2015) 7870–7876.
[180] Q. Zhao, et al., 2D MXene nanosheets enable small-sulfur electrodes to be flexible for lithium–sulfur batteries, Nanoscale 11 (17) (2019) 8442–8448.
[181] Q. Tang, Z. Zhou, P. Shen, Are MXenes promising anode materials for Li ion batteries? Computational studies on electronic properties and Li storage capability of Ti_3C_2 and $Ti_3C_2X_2$ (X = F, OH) monolayer, J. Am. Chem. Soc. 134 (40) (2012) 16909–16916.
[182] O. Mashtalir, et al., Intercalation and delamination of layered carbides and carbonitrides, Nat. Commun. 4 (1) (2013) 1716.
[183] N. Kitchamsetti, J.S. Cho, A roadmap of recent advances in MXene@MOF hybrids, its derived composites: synthesis, properties, and their utilization as an electrode for supercapacitors, rechargeable batteries and electrocatalysis, Journal of Energy Storage 80 (2024) 110293.
[184] S. Vallem, et al., Flexible MXene-conjugated polymer nanoarchitectures: current developments and future frontiers in battery technology, Coord. Chem. Rev. 510 (2024) 215778.

[185] L. Lin, et al., Flexible electrochemical energy storage: the role of composite materials, Compos. Sci. Technol. 192 (2020) 108102.
[186] T. Kshetri, et al., Recent advances in MXene-based nanocomposites for electrochemical energy storage applications, Prog. Mater. Sci. 117 (2021) 100733.
[187] C. Chen, et al., Charge transfer induced polymerization of EDOT confined between 2D titanium carbide layers, J. Mater. Chem. A 5 (11) (2017) 5260–5265.
[188] Y. Dong, et al., All-MXene-based integrated electrode constructed by Ti_3C_2 nanoribbon framework host and nanosheet interlayer for high-energy-density Li–S batteries, ACS Nano 12 (3) (2018) 2381–2388.
[189] C. Liu, et al., Robust and flexible polymer/MXene-derived two dimensional TiO_2 hybrid gel electrolyte for dendrite-free solid-state zinc-ion batteries, Chem. Eng. J. 430 (2022) 132748.
[190] Y. Tian, Y. An, J. Feng, Flexible and freestanding silicon/MXene composite papers for high-performance lithium-ion batteries, ACS Appl. Mater. Interfaces 11 (10) (2019) 10004–10011.
[191] Z. Chen, et al., Grafted MXene/polymer electrolyte for high performance solid zinc batteries with enhanced shelf life at low/high temperatures, Energy Environ. Sci. 14 (6) (2021) 3492–3501.
[192] P. Zhang, et al., A flexible Si@C electrode with excellent stability employing an MXene as a multifunctional binder for lithium-ion batteries, ChemSusChem 13 (6) (2020) 1621–1628.
[193] D. Guo, et al., Asymmetric cathode membrane with tunable positive charge networks for highly stable Li–S batteries, Energy Stor. Mater. 25 (2020) 33–40.
[194] J. Xu, et al., Redox-active Hexaazatriphenylene@MXene composite for high-performance flexible proton batteries, Compos. Part B 235 (2022) 109750.
[195] C. Wang, et al., Robust room-temperature sodium-sulfur batteries enabled by a sandwich-structured MXene@C/polyolefin/MXene@C dual-functional separator, Small 18 (43) (2022) 2106983.
[196] Y. Cao, et al., Covalently grafting conjugated porous polymers to MXene offers a two-dimensional sandwich-structured electrocatalytic sulfur host for lithium–sulfur batteries, Chem. Eng. J. 446 (2022) 137365.
[197] X.-W. Huang, et al., Pseudocapacitive enhancement for layered PI@MXene porous organic cathode in advanced lithium-ion batteries, J. Alloys Compd. 919 (2022) 165559.
[198] X. Hui, et al., In situ integrating highly ionic conductive LDH-Array@PVA gel electrolyte and MXene/Zn anode for dendrite-free high-performance flexible Zn–air batteries, Adv. Energy Mater. 12 (34) (2022) 2201393.
[199] T. Li, et al., Sandwich-structured ordered mesoporous polydopamine/MXene hybrids as high-performance anodes for lithium-ion batteries, ACS Appl. Mater. Interfaces 12 (13) (2020) 14993–15001.
[200] X. Wang, et al., Durable sodium battery composed of conductive $Ti_3C_2T_x$ MXene modified gel polymer electrolyte, Solid State Ionics 365 (2021) 115655.
[201] X. Hui, et al., Low-temperature reduction strategy synthesized Si/Ti_3C_2 MXene composite anodes for high-performance Li-ion batteries, Adv. Energy Mater. 9 (33) (2019) 1901065.
[202] F. Zhang, et al., Sandwich-like silicon/$Ti_3C_2T_x$ MXene composite by electrostatic self-assembly for high performance lithium ion battery, Energy 195 (2020) 117047.
[203] R. Zhao, et al., Self-assembled Ti_3C_2 MXene and N-rich porous carbon hybrids as superior anodes for high-performance potassium-ion batteries, Energy Environ. Sci. 13 (1) (2020) 246–257.
[204] C. Wang, S. Chen, L. Song, Tuning 2D MXenes by surface controlling and interlayer engineering: methods, properties, and synchrotron radiation characterizations, Adv. Funct. Mater. 30 (47) (2020) 2000869.
[205] B. Anasori, et al., Control of electronic properties of 2D carbides (MXenes) by manipulating their transition metal layers, Nanoscale Horiz. 1 (3) (2016) 227–234.
[206] A. Agresti, et al., Titanium-carbide MXenes for work function and interface engineering in perovskite solar cells, Nat. Mater. 18 (11) (2019) 1228–1234.
[207] F. Ming, et al., Porous MXenes enable high performance potassium ion capacitors, Nano Energy 62 (2019) 853–860.
[208] L. Zhao, et al., Interdiffusion reaction-assisted hybridization of two-dimensional metal–organic frameworks and $Ti_3C_2T_x$ nanosheets for electrocatalytic oxygen evolution, ACS Nano 11 (6) (2017) 5800–5807.